Tactile Feedback Systems

Michael Fritschi, Martin Buss
Institute of Automatic Control Engineering (LSR)
Technische Universität München
D-80290 München, Germany
Email: michael.fritschi@ei.tum.de
www.lsr.ei.tum.de

Knut Drewing, Regine Zopf, Marc O. Ernst
Max Planck Institute for Biological Cybernetics
Spemannstr. 38
D-72076 Tuebingen, Germany
Email: marc.ernst@tuebingen.mpg.de
www.kyb.mpg.de

***Abstract*— Tactile feedback is among haptics one of the more recent modalities for human-system interaction. Research in tactile feedback using pin-array type actuators has been going on during the past 10 years or so. A survey about technological achievements, human sensing capabilities, and psychophysical evaluation in this area is presented. Then the focus is on novel approaches in actuator technology and tactile feedback systems providing shear force (tangential force to the finger-tip).**

I. Introduction

The human tactile perception is a complex combination in sensing various physical information from our environment. While manipulating an object with our hand, we can perceive reaction forces, pressure, temperature or pain using different receptors/nerve-endings beneath our skin. Research in tactile feedback systems in general try to recreate these environment in a technical way either in form of a telepresence scenario [1] or based on virtual reality [2].

Most approaches in technical realization of tactile displays followed the idea to display the shape of an object, that has to be explored as a kind of spacial 'picture'. Similar to a Braille generator, displaying script information for blind people in a tactile way to the human finger pulp, wherefore in many cases an array of movable pins is used. Each of these pins must independently be able to fulfill movement normal to the human skin (mostly toward the finger-tip of the index finger). To reach a realistic impression of the generated object, the density and performance of the pins have to be adapted to the performance of the human tactile perception system (mechanoreceptors). Based on this principle of so called normal force displays, several tactile displays have been build [3]–[7]. More recent studies pointed out, that considering the forces tangential to the human skin could be also important. This forces arise for instance while sliding with the finger pulp over a surface. Moreover, this stimulation of shear force seems to have more influence to the tactile perception as expected. Meanwhile there are some Displays providing shear force in different ways, like pin based displays [8], [9], displays that are designated to display slip at the fingertip [10], [11] or displays specialized to provide stimuli of object contact and edges [12]. Most of this devices are in a prototype state or used to explore the influence of shear force to the human perception.

A common problem on these existing tactile displays from the technical point of view is the demand on high pin density at a concurrently large excursion and high frequencies of pin movement.

However, there are still some unanswered questions on the perceptual side. The discrimination performance of humans to distinguish between different direction of shear force provided to the skin and the perceptual integration (based on the hypothesis of [13]) of multi-pin movement, are only two of those questions, such as will be discussed in this paper.

To approach these problems in a rambling way, our research in tactile feedback systems can be split into two main directions:

- **Advancement in actuator technologies.** In this issue we explore new appendages to solve the problem of providing the necessary functionality of tactile stimuli in a technical way, by combining common actuator technology and micro-mechanical solutions to a combined actuator system adapted to the psychophysical characteristic of the human tactile perception.
- **Illusion based tactile displays** At this direction we aspire novel concepts in tactile displays by an iterative process between technical design and psychophysical evaluation. In a first approach we build a tactile shear force prototype device for psychophysical evaluation of discrimination performance regarding the human tactile perception of shear force and do some preliminary studies exploring the perceptual integration of multi-pin movement tangential to the skin.

After an introduction of the human cutaneous sense in section II the short overview of common used actuator technologies for tactile displays is given. Thereby the focus is only on available actuators that are commonly in use for tactile displays. Regarding the research in new actuator designs, this paper presents the first concept of combined pin actuator, using two piezo crystal actuators, that are coupled by an mechanical lever system described in chapter IV. On our direction to find illusion based tactile systems, the design of a novel tactile shear force prototype device, as well as first evaluations regarding the human discrimination in shear force direction and the integration of multi stimulus in the human brain is presented in chapter V.

TABLE I

FUNCTIONAL FEATURES OF THE FOUR-TYPES OF MECHANORECEPTORS BENEATH THE HUMAN HAND. ADAPTED FROM [17] [18] [19]

Features	Meissner Corpuscles	Pacinian Corpuscles	Merkel's Disks	Ruffini Corpuscles
Location	Superficial dermis	Dermis and subcutaneous	Basal epidermis	Dermis and subcutaneous
Rate of adaptation	Rapid (RA-I)	Rapid (RA-II)	Slow (SA-I)	Slow (SA-II)
Spatial resolution	Poor	Very poor	Good	Fair
Mean receptive area	$13\,\mathrm{mm}^2$	$101\,\mathrm{mm}^2$	$11\,\mathrm{mm}^2$	$59\,\mathrm{mm}^2$
Sensory units	$43\,\%$	$13\,\%$	$25\,\%$	$19\,\%$
Response frequency range	$10-200\,\mathrm{Hz}$	$70-1000\,\mathrm{Hz}$	$0.4-100\,\mathrm{Hz}$	$0.4-100\,\mathrm{Hz}$
Min. threshold frequency	$40\,\mathrm{Hz}$	$200-250\,\mathrm{Hz}$	$\sim 50\,\mathrm{Hz}$	$\sim 50\,\mathrm{Hz}$
Physical parameter sensed	Velocity, local shape, slip	Vibration, slip, acceleration	Local shape, pressure	Skin stretch, locale force
Force thresholds	$0.58\,\mathrm{mN}$	$0.54\,\mathrm{mN}$	$1.3\,\mathrm{mN}$	$7.5\,\mathrm{mN}$

II. HUMAN CUTANEOUS SENSE

The skin is the largest receptor surface of any of the human senses. It gives us the possibility to perceive various kinds of environmental impressions as touch (pressure), temperature, cold, pain, tickle, and itch. This different perceptual qualities are described by the general term *cutaneous senses*. Fig. 1 shows the schematic structure and

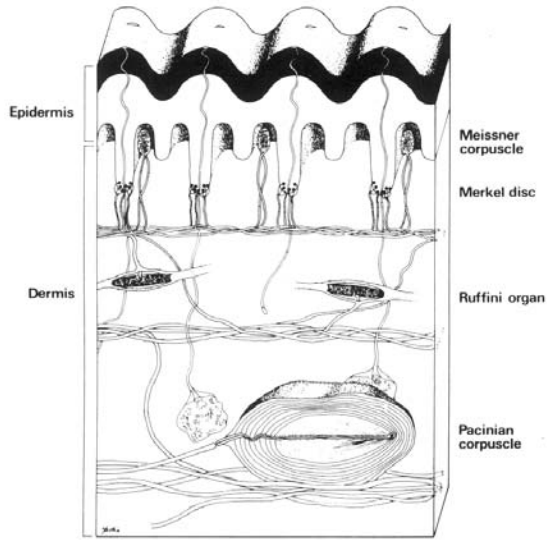

Fig. 1. A cross section of the skin, showing the layers and the receptors. Adapted from [14]

position of the four types of touch receptors within the human glamorous skin, which are called the *mechanoreceptors*[1]. They can be seen as specialized nervous cells or neurons for transmission of tactile information into fibers. This information in form of electrical pulses converge via second-order neurons into the central nerve system [15]. The mechanoreceptors are generally divided in two classes, *rapidly adapting* (RA)[2] and *slowly adapting* (SA) mechanoreceptors. RAs in general response on temporal changes in force indentation e.g. at the phase of contact or release of the skin with an object. The SAs respond also on constant force exertion to the skin [14] [16]. The two main classes of mechanoreceptors (RA, SA) are divided into two sub types characterized by numbers. The Meissner corpuscles, located in the lower part of the epidermis (Fig. 1), respond in a frequency range of $10-200\,\mathrm{Hz}$ and optimal to vibrations at frequencies of around $40\,\mathrm{Hz}$ they are assigned to the RA-I mechanoreceptor type. Pacinian corpuscles, located between the epidermis and the dermis are associated to the RA-II receptor type. They respond on a frequency spectrum of $70-1000\,\mathrm{Hz}$ with an optimal response in the frequency band of $200-250\,\mathrm{Hz}$. Both SA mechanoreceptor types are located in deeper layers of the dermis and respond on frequencies up to $100\,\mathrm{Hz}$ whereas Merkel's disks are assigned to the SA-I and Ruffini corpuscles to the SA-II receptor type [17] [18]. Tab. I shows a comparison of the described bio-physical features collected from different investigations. The obtained results about the mechanoreceptor density are related to the human hand. The human hand contains about 17000 mechanoreceptive units innervating the glabrous skin [20]. Its most sensitive area is located in the finger pulp, which has with $97\,\%$ of SA-I units, $82\,\%$ of SA-II units, $76\,\%$ of RA-I units, and $30\,\%$ of RA-II units one of the highest receptor density regarding the human skin.

Most of this mechanoreceptor type specific values originate from neurological measurements, done by direct recording the single afferent units with so called turgsten needle electrodes, which are percutaneously inserted in a region about $10\,\mathrm{cm}$ above the elbow [21]. With his method it is possible to locate and record the response of nearly every mechanoreceptor.

The tactile stimulus provided to the human skin cannot be directly assigned to a type of mechanoreceptor. One reason for instance is the overlapping in response frequency (Tab. I). This values let assume, that the quality of cutaneous perception is caused by the correlation of inputs from different receptor types. Thus frequencies in the range of

[1]The receptors which are responsible for perception of temperature and pain are not discussed in detail here.

[2]In some publications the equal notation FA (*fast adapting*) is used.

$50 - 230$ Hz are responded by mostly all receptors with rising sensitivity and perceived as vibration. Frequencies above 230 Hz can only be acquired by RA-II receptors and due to their poor resolution it is difficult to localize the source of vibration. Investigations referenced in [18] note that the receptive areas and frequency response rate indicate that a single vibratory stimulus at the fingertip can be used to present vibration information for frequencies above 70 Hz. This psychophysical characteristic could play an important role on design of a tactile device, because of reducing actuator performance.

The force thresholds of the mechanoreceptors, shown in Tab. I are mainly related to indentation forces normal to the skin. An exception from the bio-physical point of view are the Ruffini corpuscles. Their long axes are usually oriented parallel to the skin surface, as shown in Fig. 1. This let assume, that they are able to transmit a neural image of skin stretch. The high force thresholds of these SA-II receptors to punctuate stimulation normal to the skin may be caused by these properties [19].

TABLE II

TACTILE SENSATION AND MECHANICAL IMPEDANCE OF THE HUMAN FINGER. ADAPTED FROM [22] [23]

Indentation Threshold ($0.3\,\mathrm{mN/mm^2}$)	
Static	$20\,\mu$m
$10\,$Hz	$10\,\mu$m
$250\,$Hz	$0.1\,\mu$m
Feature Detection	
Texture	$0.075\,\mu$m (lat.)
Single dot	$2\,\mu$m
Detecting features (NF)	$0.4 - 1.1\,$N
Temporal Solution	
Successive tap time	$10\,$ms
Bandwidth sense	$0 - 1000\,$Hz
Reaction time	$70\,$ms to $500\,$ms
Spatial Resolution	
Lateral localization	$0.15\,$mm
Lateral 2-point limen	$1 - 2\,$mm
Mechanical Impedance (static)	
Range of finger pat indentation	$\sim 3\,$mm
Initial contact $(0 - 1\,\mathrm{mm})$	$\sim 0.1\,\mathrm{N/mm}$
Further indentation $(1 - 2\,\mathrm{mm})$	$\sim 0.4\,\mathrm{N/mm}$
Further indentation $(2 - 3\,\mathrm{mm})$	$\sim 1.0\,\mathrm{N/mm}$
indentation $> 3\,$mm	$10 - 100\,\mathrm{N/mm}$
Lateral indentation	$0.53\,\mathrm{N/mm}$

Tab. II shows some general thresholds related to the skin of the human index finger pulp, based on different psychophysical investigations. As expected by the allocation and characteristics of the mechanoreceptors, the indentation threshold normal to the skin surface decreases by an increase of stimulation frequency. Additionally there has been found a coherence between the sensibility of indentation and the cross section of the used contactor [24]. Thus, lowering the cross section from $8\,\mathrm{cm}^2$ to $0.02\,\mathrm{cm}^2$ causes an increase of indentation sensibility by about 30 times. The feature detection resolution of a surface is very high while strokeing the finger pulp about an object, whereas the spatial resolution in the static case is comparatively bad. This is also caused by the fact that the vibrations caused by friction on sliding the finger at an object can sensed very well by nearly all types of mechanoreceptors. Investigations in mechanical impedance of the skin at the finger pulp has been result a nonlinear increase of impedance on deeper ranges of indentation until a maximum indentation of approx. $3\,$mm, constraint by the compression of the tissue between contact surface and bone of the finger. Studies of lateral indentation thresholds [23] identified a much higher but mostly constant mechanical impedance of approximately $0.53\,\mathrm{N/mm}$. However, the tangential displacement thresholds of the finger pad is only 0.6 times as high as the reference normal displacement.

In order to produce a realistic tactile impression of the environment it is probably as important to provide forces lateral to the human skin, so called shear forces. This is particularly reasonable when considering perceptions evoked by movements of the skin relative to the environment, e.g. when stroking with the finger across a surface. The perception of movement across the skin has been demonstrated to rely upon skin stretch probably mediated via SA 2 receptors as well as upon the translation of a stimulation probably mediated by FA 1 receptors. Human perception here seems to be particularly sensitive to the stretch component [25]. To give another example, shear forces do also play an important role in applying a precision grip. When gripping and lifting a fragile object like an egg, grip forces should be sufficiently large to avoid slip of the object, but also sufficiently small to avoid damage to the object. FA 1 receptors in the skin have been demonstrated to immediately feed back slip and, thus to allow for a precise force control [26]. Note that current tactile devices are most likely to address other types of receptors in the skin, namely SA 1 (shape devices) and FA 2 (rapid vibrotactile devices) receptors. An impressive movement illusion evoked by shear forces can be easily generated attaching a comb to the finger and sliding a pencil along its teeth [27]. This illusion further corroborates the assumption that shear force plays an important role for human tactile perception.

The attempt on technical side is on the other side constrained on the present actuator technology, while there is no actuator available that can satisfy all this demands on performance at present. One approach to compensate this effort is finding a way to cheat our tactile perception in a way to reduce actuator capacity. Results in this direction demonstrate that the display quality of tactile displays depends strongly on the demands of the application [28]. Furthermore recent psychophysical integration hypothesis [13] may indicate new possibilities for illusion based tactile displays.

III. ACTUATOR TECHNOLOGIES FOR TACTILE DEVICES

The choice of actuator is an essential decision for the design of a tactile display. As the findings in the previous chapter let assume, there is a necessity of a very high power density on the mechanical side, to provide a realistic stimulation of the cutaneous sense. For instance

an ideal display which exerts normal forces to the fingertip requires $50\,\mathrm{N/cm^2}$ peak pressure, $4\,\mathrm{mm}$ stoke, and $50\,\mathrm{Hz}$ bandwidth; that is a power density of $10\,\mathrm{W/cm^2}$ with an actuator density of 1 mm^{-2} [29][3]. This ideal is far from what can be achieved with current actuator technologies.

In this section a brief survey of actuators for tactile displays which are available or under development is given. A more detailed summary about new materials, that are predestined for design of tactile displays but currently in development can be found in [30].

A. Electromagnetic actuators

In robotics the by far most commonly used *DC* (direct current) motor is related to the type of electromagnetic actuators. It uses a combination of permanent magnet, coils and a commutator to produces a rotating electromagnetic field, that produce a rotatory motion at the output shaft of the motor. Attached reduction gears are generally used to increase the torque but decrease the speed. DC motors in combination with encoders for position measurement and a position control, so called *servo motors*, are available in different sizes and provide a good position accuracy. One disadvantage of DC motors in general is that the produced rotary motion must be transformed in the necessary linear motion by rocker arms or combinations of screws and nuts.

TACTACT4 is an example for a tactile normal force display which uses gear-less DC motors [31]. Thereby the rotatory motion of the position controlled motors is transformed into linear motion by excentric discs to whose circulation edges guided the pins in linear direction. Each pin of the 2×2 pin-array display can reach a maximum stroke of $4\,\mathrm{mm}$, continuously controllable in position. It provides forces up to $2.5\,\mathrm{N}$, and has a mechanical bandwidth of $> 60\,\mathrm{Hz}$. Irrespective of the very large pin spacing of $8\,\mathrm{mm}$, it provides a highly realistic stimulus for some applications, like the palpation of the human skin according to detect some medical objects (e.g. tumors).

Another example using DC servo motors for tactile displays is presented in [32]. This display consists of 36 pins in an order of a 6×6 matrix with a pin spacing of $2\,\mathrm{mm}$. It provides tactile force normal to the fingertip, with continuously controllable pin deflections of $2\,\mathrm{mm}$. To actuate the pins, commercial radio-controlled (RC) servo motors have been used. Those motors come with a embedded position sensor and a closed-loop position controller. This device provide frequencies up to $7.5\,\mathrm{Hz}$ for the maximum pin deflection of $2\,\mathrm{mm}$ and up to $25\,\mathrm{Hz}$ for amplitudes less then $0.75\,\mathrm{mm}$.

Solenoids actuators belong to the class of electromagnetic actuators that can produce direct linear motion. In principle they consist of a coil of wire, generating a magnetic field, and an iron component that moves towards the coil and thus can implement e.g. pin motion. Based on the physics of the electrical field that occurs on energize the coil, the relation between movement and the attracting force of the iron is highly non-linear. Due to this fact it is very difficult to implement a position control-loop. At his reason solenoids are mostly used for vibrotactile displays.

So, for instance in [33] [34] an one pin vibrotactile actuator, mounted to the kinesthetic display (PHANToM^{TM}) is described. This solenoid actuator is attached to the operator's thimble providing a planar tactile stimulus with frequencies up to $200\,\mathrm{Hz}$. The stroke position of the actuator is controlled by a PI controller.

A modified principle of solenoid actuators is used at the pin matrix based tactile display TACTACT36 [35]. In opposite to the general principle, on these actuators the coil is attached to the moving part of the mechanism, so activation of the coil causes an attraction of the electromagnetic rocker lever to the fixed component. The display contains a 6×6 tactile normal force actuator array. Since it has no position/force control the actuator pins can only be driven in binary mode. The pins can exert an initial forces of $0.8\,\mathrm{N}$ and continuous forces of approximately $4.5\,\mathrm{N}$ at the fixed maximum stroke of $1.6\,\mathrm{mm}$. The pins can be driven independently and reach frequencies larger than $100\,\mathrm{Hz}$.

The *voice coil* actuators are based on the well known principle used for loud speaker chassis. As the fixated part, a cylindric permanent magnet establishes a static magnetic field. The coil, circular wounded around the permanent magnet with a small gap between magnet and coil, represents the moving part of the actuator. A current applied to the coil, produces a change in the magnetic field, thus resulting a force on the coil, that causes linear motion of the moving part [36]. The so generated force is proportional to the magnetic field of the permanent magnet whereby a simple force control loop is possible. The moving part (coil) mostly has a low mass and can in general provide larger forces than solenoids. Voice coil actuators have no mechanical hysteresis, no force or torque ripple, and no backlash. Because of the problems with position control of various static excursions they maybe used mainly for vibrotactile displays.

B. Pneumatic actuators

Pneumatic actuators use the pressure or flow of the air to drive pins or inflate air chambers. The benefit of pneumatic actuators is that the compressor which generates the pressure can be placed at peripheral locations. Therefore they can provide a good local power density by using simple components. Disadvantages are the non-linearities and thus difficulties in control of either pressure or flow. Further, aerodynamic effects cause limitations on actuator bandwidth. In [37] a 5×5 chamber pneumatic display is shown. A 4×4 pin display driven by pneumatic cylinders is presented in [38].

C. Piezoelectric actuators

Piezoelectric actuators (PTZ) based on the phenomenon of the deformation of a quartz crystal caused by an electrical field. Two main types of piezo actuators for longitudinal

[3]This example is calculated to stimulate the SA-I mechanoreceptors with the highest mechanoreceptor density ($70\,\mathrm{cm}^{-2}$) at the finger.

motion are available: high voltage PTZs requiring about 1000 Volt for full extension, and low voltage (multilayer) PTZs requiring about 100 Volt for full motion. Multilayer designs, constructed from 20 to $100\,\mu$m layersin low voltage piezos, allow achieving a relative expansion (strain) up to $0.2\,\%$, if both the regular and inverse electric field is used. Drift and hysteresis of piezo actuators can be eliminated using position feedback control so that a high position accuracy can be achieved. Piezoelectric actuators can excite very high frequencies up to several kHz. To enhance the displacement range two thin piezo ceramic strips can be connected together so that one of them contracts while the other expands. The so called *bimorph design* is similar to the bimetallic gauge.

Piezoelectric actuators are used in [6] for vibrotactile texture exploration attached to PHANToM^{TM}. Each pin of the 5×2 array is driven by a bimorph-like piezoelectric actuator at the frequency of 250 Hz and a maximum amplitude of $22\,\mu$m.

A piezoelectric actuator based tactile shear force display is presented in [27]. A field of 64 upstanding piezoelectric actuators initialize a coupled swing motion of the 112 skin contactors above, thus a differential displacement of two neighboring actuators determine a lateral displacement on the top of the contactor.

D. Shape memory alloys

Wires or pins manufactured with *Shape memory alloys* (SMA) can easily be deformed when they are cold. While heating the alloy force the wire to return into prior form, so it is able to "remembering" his original shape. The most common used SMA is nickle titanium. As direct drive linear actuator SMA can exert thrusts up to $200\,\text{N/mm}^2$. The recovery strain is in the order of $5-8\%$, and thus very large compared with piezoelectric actuators. Although SMA actuators appear to have the highest force per unit area and large displacement, several factors make them difficult to use for tactile displays. The main disadvantages are slow speed of response, fatigue problems (short lifetime) and cooling problems.

A pin array based tactile normal force display with 64 contactors is presented in [39]. An approach in control of a SMA wires based tactile display is presented in [40]. The contactor of this display reached a bandwidth of $7-8$ Hz (on -3 dB). Furthermore, there are some interesting approaches in control and design for using SMA as an actuator technology [41] [42].

E. MEMS actuators

Micro-electromechanical systems (MEMS) technology provides highly integrated mechanical structures resp. actuators. The mayor technology used for MEMS actuators is typically magnetic, electrostatic or thermal.

An approach of a MEMS technology based display is described in [43]. This tactile normal force display provides with 24 actuators cm^{-2} a very high pin density. Unfortunately no performance data are available because it is still under development [4].

IV. Combined pin actuator

The chapter above shows, nearly every known tactile display uses one actuator per pin to generate a tactile stimulus to the human skin. Moreover is indicated, that no current actuator principle exists to provide the affordable power density or mechanical compactness and thus could be used to display the necessary psychophysical qualities for a high fidelity tactile stimulus. A way to improve this could be an adaption of the mechanical actuator performance to these psychophysical necessity. Our approach in this case is to use two single actuators, optimized to an individual range of tactile stimulation, and combine them in serial manner to an adapted combined pin actuator. So, the subject of this chapter is the design and realization of this combined pin actuator. After the target specification, derived from the psychophysical data found in chapter II the design and the modules of the combined pin actuator are described and evaluated.

A. Target specification

According to the psychophysical data, listed in Tab. II the general target specification of the combined pin actuator in terms of excursion, frequency, and force can be stated as followed:

- **Excursion:** The overall excursion is physically limited by the compression of the tissue between the surface and the bone of the index finger. The upper limit is approximately 3 mm.
- **Frequency:** The frequency bandwidth of the cutaneous perception is about $0-1000$ Hz. The sensitivity of indentation increases until a maximum at around 230 Hz [17].
- **Force:** In the static case the maximum force is required at an indentation of 2.5 mm. With an impedance of $1\,\text{N/mm}$ a force of $3\,\text{N}$ is needed.

Towards the objective to build up a pin actuator with two actuator technologies the major question is the segmentation of tasks for the specific actuators. Fundamentally, there are two qualities of stimulation of pin actuated systems attached to the skin: amplitude and frequency of the pin. Investigations based on psychophysical observations showed that there is a threshold in detecting vibrations [15]. The lower limit for the fuse of pulses into one continuous sensation (vibration) can be considered to be in the range of $10-80$ Hz. In consideration of the general findings in chapter II it has been found that a reasonable breakdown of actuator tasks can be made by splitting the frequency domain per actuator. The resulting actuator modules and their functionality ranges can be stated as follows:

- **Low frequency actuator:**
  Provide large excursion of up to 3 mm in a frequency range of $0-70$ Hz.

[4] http://www.ri.cmu.edu/projects/project_470.html

- **High frequency actuator:**
  Provide vibro-tactile stimulations with excursions up to $20\,\mu$m in the frequency range of $70 - 1000\,$Hz.

In the case of the low frequency actuator, the fact of rapid decrease of threshold detection in the frequency domain ($2\,\mu$m at $70\,$Hz) [15] has been used to reduce excursion. The estimated value in excursion of 10 times higher than the threshold is based on experiments made in [44], where a stimulus with an amplitude of 8 times higher regarding the threshold at a frequency of $70\,$Hz can be associated with a hard brush.

B. Low frequency module

Referring on inquires of actuator principles stack piezo crystals seems to provide the best trade-off between performance and power density for the low frequency module. After investigations in off-the-shelf stack piezo actuators in terms of size, force, and excursion we chose a stack piezo from Piezomechanik GmbH.

TABLE III
STACK PIEZO DATA

Type	PSt $150/5 \times 5/20$
Max. excursion	$30\,\mu$m
Max. force	$1800\,$N
Stiffness	$60\,$N/μm
Resonance freq.	$35\,$kHz
Supply voltage	$-30 - 150\,$V
El. capacity	$1800\,$nF
Size (stack)	$5 \times 5 \times 18\,$mm
Weight (stack)	$5\,$g

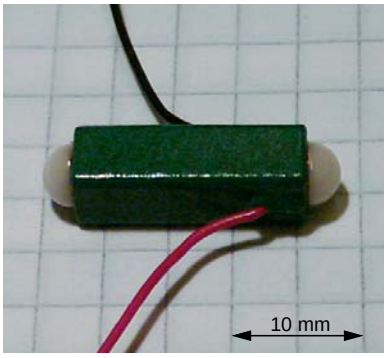

Fig. 2. Stack piezo actuator

Tab. III shows the data of the selected stack piezo. A feature of this stack piezo series is the large expansion ratio of $0.16\,\%$. For better load transmission a version with half spherical ceramic caps on bottom and top of the stack (Fig. 2) is chosen, that increase the fitting size up to $23\,$mm.

Piezo crystals have a linear force-excursion characteristic between maximum force on zero excursion and zero force on maximum excursion. Following calculations on mechanics are based on half the max. excursion ($15\,\mu$m). In this range the piezo can provide forces up to $900\,$N

To reach a pin excursion of $2.5\,$mm, a mechanical system of levers has to transmit the movement of the actuator with a ratio of $166.6\overline{6}$. The simplest way to realize this is to use a lever system shown in Fig. 3. Based on a minimum distance of $\overline{\mathrm{AB}} = 3\,$mm, predetermined from the deviations of the piezo, the length of the lever $\overline{\mathrm{AC}}$ rises up to 50 cm. That would dissent consequently the demand of compactness.

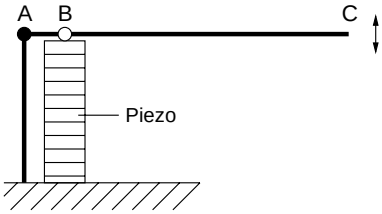

Fig. 3. One lever transmission

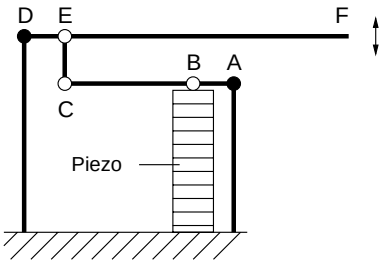

Fig. 4. Cascaded two lever transmission

Fig. 4 shows the schematic structure of the resulting cascaded two lever transmission system. Revolute joints are displayed as circles; the filled circles show joints with fixed axis. The first stage (A,B,C) is enhanced by a second (D,E,F), acting the opposite direction to reduce the overall size of the lever and increase compactness of the module. The transmission ratio of the combined lever system can be calculated to:

$$i_{\mathrm{BF}} = i_{\mathrm{BC}}\, i_{\mathrm{EF}} = \frac{\overline{\mathrm{AC}}\,\overline{\mathrm{DF}}}{\overline{\mathrm{AB}}\,\overline{\mathrm{DE}}} = 166.6\overline{6}. \tag{1}$$

With the additional constraints of:

$$i_{\mathrm{EF}} = 2\, i_{\mathrm{EF}}, \quad \overline{\mathrm{DE}} = 3\,\mathrm{mm}, \tag{2}$$

the lever lengths result to:

$$l_{\mathrm{lower}} = \overline{\mathrm{AC}} = 27.38\,\mathrm{mm}; \quad l_{\mathrm{upper}} = \overline{\mathrm{DF}} = 54.75\,\mathrm{mm}. \tag{3}$$

Based on this kinematic dimensioning a mechanical construction has been found. A major point is to find a solution for the construction of the joints A, C, D, E and F. After a comparison between different standard techniques in fine mechanics [45] the method of solid state joints has been selected. These joints are realized by elastic bending of its thin paths at their pivot points. They need no assembling or adjustment, have no abrasion, nearly no friction and zero backlash. The disadvantage of this technique, the high restoring force, can be used to provide the necessary preload for the stack piezo. As a consequence of this design, the whole lever transmission mechanism has to be built out of one piece.

Fig. 5 shows the first layout of the cascaded two lever system designed on the described principle. The picture

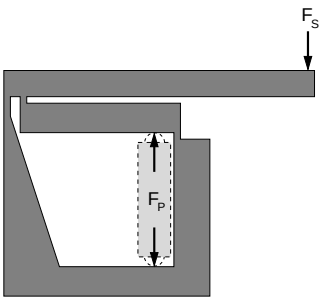

Fig. 5. First layout of combined lever system

displays the side view of a cut out plate with a thickness of ~ 2 mm. The lever system must be designed this way, that the piezo (hinted pictured) fits itself with some initial load. At the endpoint of the second lever the pin can be attached to use the amplified motion in vertical direction. The force of the stack piezo F_P and the load of the pin F_S, caused by skin impedance, are displayed at their action points.

On further steps to analyze the range of motion and the tension at the bending joints the finite elements method (FEM) is used to optimize shape and functionality of the combined lever system. As simplification for the FEM computation only the stack piezo load in direction of the first lever has been considered. This can be made because on the bottom point of contact no deformation or critical stress is expected.

Fig. 6 shows the results of the first FEM calculations. The left picture displays the deformation of the lever system at maximum load generated by the stack piezo. Furthermore, the arrangement of the notes used for the computation can be seen. The colored picture on the right side of Fig. 6 displays the stress fields with a table of the color related stress forced aside. For the first three design loops quality steel (C55) with a thickness of 2 mm has been used. This steal has an elastic modulus of $E = 210000\,\frac{N}{mm^2}$ and a fatigue resistance of $500\,\frac{N}{mm^2}$. With this raw material values the deviations of the three bending joints has been pre-calculated to $1 \times 1 \times 2$ mm and the cross-sectional area of the levers to 5×2 mm (thickness of lever system plate $d = 2$ mm). First calculation results an excursion of $91\,\mu$m at the end of the second lever, activated by a piezo excursion of $23\,\mu$m at a force of 470 N. The reason for this bad excursion are the accidental bending behavior of the levers and the body. The stress field picture indicates low tensions in the joints and as a consequence to less bending in the joints. It displays low stress values at some places to adapt the shape as a result of the stress field.

During some iterations in design regarding FEM calculations, some basically chances of the combined lever system has been made:

- Decrease of thickness of the base plate down to 1.6 mm.
- Redesign of shape, based on stress field results of further designs.
- Decrease of cross-section area length of the bending joints.
- Elongation of upper and lower lever, to adapt transmission ratio.

The resulting values in the area of the bending joints stress field are shown in Fig. 7. The movement at the end of the second lever raises up to 1.6 mm at a stack piezo excursion of $25\,\mu$m. In this maximum position the lever system provides preloaded force of 310 N to the stack piezo. The stress field picture in Fig. 7 shows, that the maximum stress areas at the bending joints are safely in the non deformable range when using heat-treated steel (50CrNi4) with a fatigue resistance up to $900\,\frac{N}{mm^2}$.

The body of the low frequency module was manufactured based on the final design loop by the method of wire-electro discharge machining.

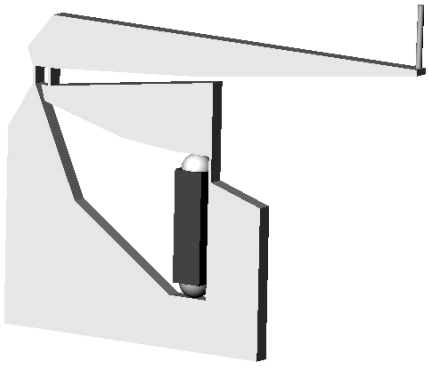

Fig. 8. Final combined lever system with stack piezo

Fig. 8 shows the body of the combined lever system with attached stack piezo. At the end of the second lever the fixation point for the pin is indicated.

Position control

In consideration of the expected dynamic behavior of the described lever system body, as also the hysteresis in the response behavior of the stack piezo actuator, there is a need for a closed-loop position control for the excursion of the pin. For the control-loop a sensor has been attached to the end of the second lever. This self-made sensor is based on a *PSD* (position sensitive diode) from IC-Haus Ltd. (`http://www.ichaus.com`). With this PSD the position of an infra red light spot can be detected within an area of 2.6×0.88 mm. The light spot is generated by aperture with a diameter of 0.3 mm in a flat aluminum stick, which is attached to the end of the lever system body. The sensor is fixed to the ground plate and receives the moving light spot caused by shading effects of the aperture. For source of light a pulsed infra red diode at the opposite of the sensor is attached.

Modeling

A model for the combined rocker lever system is needed for analyzing the mechanic behavior in view of the design of a position control algorithm and as shown later as a reference model for the finally used observer based control strategy. Fig. 9 shows a schematic construction of

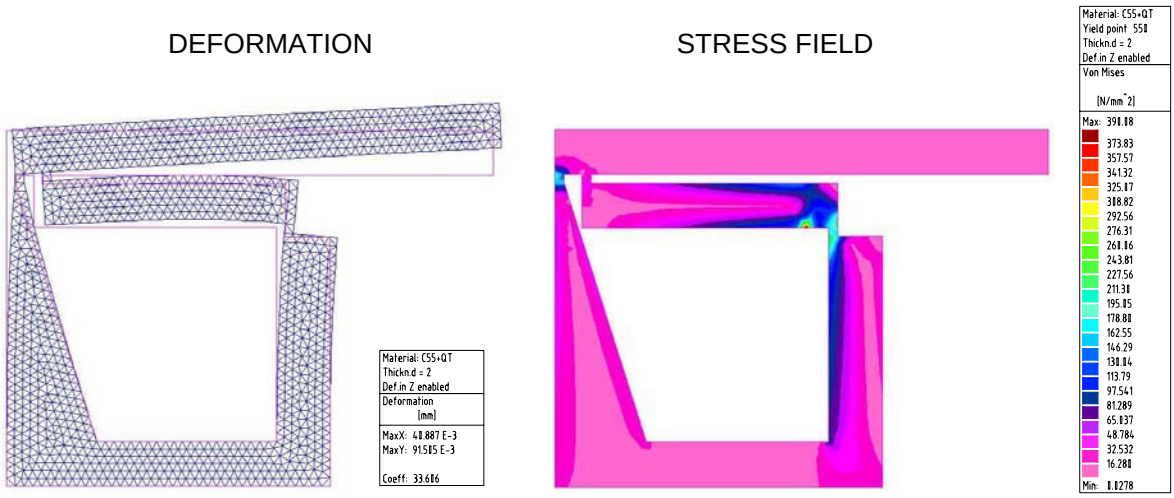

Fig. 6. First FEM - design loop of the combined lever system

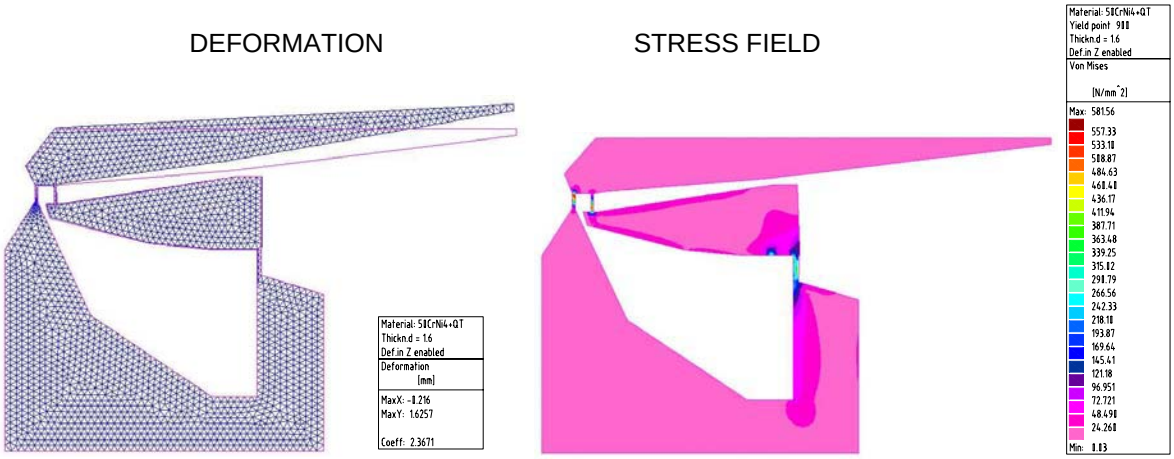

Fig. 7. Fourth FEM - design loop of the combined lever system

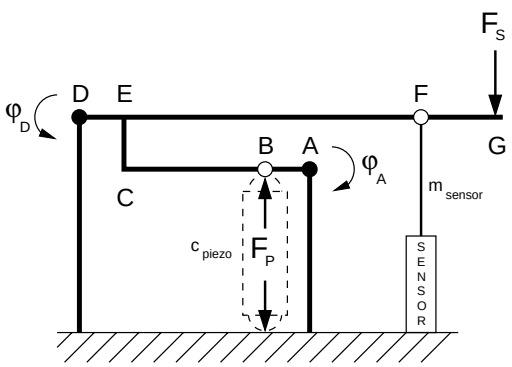

Fig. 9. Mechanical model

the system with external acting forces. The force of the stack piezo (F_{P}) represents the control variable whereas F_{S}, caused by the impedance of the human skin, acts as disturbance variable to the control system. Compared with Fig. 4, used for calculating the kinematics, the connections at the points C and E are fixed like at the real system, because of modeling as bending beam. Dynamic relevant components, like the sensor rod at point F and the pin rods at G, shown in Fig. 9, have been considered in the computation.

Thus, the equations of motion can be calculated by solving the Lagrangian differential equations:

$$\frac{d}{dt}\left(\frac{\partial L}{\partial \dot{q}_i}\right) - \frac{\partial L}{\partial q_i} + \frac{\partial R}{\partial \dot{q}_i} = Q_i, \tag{4}$$

with the Lagrangian equation:

$$L = T - V. \tag{5}$$

Where T represents the kinetic energy, V the potential energy of the considered mechanical system, R contains dissipation energy (e.g. in consequence of damping) and Q_i the external load to the mechanical system, related to the corresponding generalized coordinate q_i.

The generalized coordinates q_i are defined by the angles of the lower (φ_{A}) and upper (φ_{D}) lever to the vector $\boldsymbol{q}$ as:

$$\boldsymbol{q} = \begin{pmatrix} \varphi_{\mathrm{A}} \\ \varphi_{\mathrm{D}} \end{pmatrix} \tag{6}$$

Regarding the generalized coordinates $\boldsymbol{q}$, the equations of the kinetic energy T, the potential energy V and the

dissipation energy R of our mechanical system in general form are given to:

$$\begin{aligned} T &= \frac{1}{2}\,J_{\text{AC}}\,\dot{\varphi}_{\text{A}}^2 + \frac{1}{2}\,J_{\text{DG}}\,\dot{\varphi}_{\text{D}}^2 \\ &\quad + \frac{1}{2}\,m_{\text{sensor}}\,l_{\text{DF}}^2\cos^2(\varphi_{\text{D}})\,\dot{\varphi}_{\text{D}}^2 \qquad (7) \\ V &= \frac{1}{2}\,c_{\text{A}}\,\varphi_{\text{A}}^2 + \frac{1}{2}\,c_{\text{D}}\,\varphi_{\text{D}}^2 \\ &\quad + \frac{1}{2}\,c_{\text{CE}}\,(\varphi_{\text{A}} - \varphi_{\text{D}})^2 + \frac{1}{2}\,c_{\text{piezo}}\,l_{\text{AB}}^2\sin^2(\varphi_{\text{A}}) \\ &\quad + m_{\text{AC}}\,g\left[\frac{1}{3}\,l_{\text{AC}}\sin(\varphi_{\text{A}}) + y_{\text{AC}}(\cos(\varphi_{\text{A}}) - 1)\right] \\ &\quad + m_{\text{DG}}\,g\left[\frac{1}{3}\,l_{\text{DG}}\sin(\varphi_{\text{D}}) + y_{\text{DG}}(\cos(\varphi_{\text{D}}) - 1)\right] \\ &\quad + m_{\text{sensor}}\,g\,l_{\text{DF}}\sin(\varphi_{\text{D}}) \qquad (8) \\ R &= \frac{1}{2}\,d_{\text{A}}\,\dot{\varphi}_{\text{A}}{}^2 + \frac{1}{2}\,d_{\text{D}}\,\dot{\varphi}_{\text{D}}{}^2 + \frac{1}{2}\,d_{\text{CE}}\,(\dot{\varphi}_{\text{A}} - \dot{\varphi}_{\text{D}})^2 \qquad (9) \end{aligned}$$

With J the inertia coefficient, g gravitational acceleration, c stiffness coefficient, d damping coefficient, and m the masses, referring to the schematic in Fig. 9. The values y_{AC} and y_{DG} represent the vertical position shifts of the centers of gravity from the corresponding centers of rotation.

In the energy terms (7)-(9) the following simplifications have been made:

- The kinetic energy of the stack piezo and the joints (beams) are neglected in (7).
- Only the vertical velocity has been considered in (7)
- The potential energy of the piezo body has been neglected in (8).
- Because of optimization with the FEM in the section above, the lower and upper lever are supposed as rigid bodies, so their dissipation energy have been neglected in (9).

The solution of the Lagrangian differential equations Eq. (4) including the external load, caused by the piezo stack, of $Q_{\varphi_{\text{A}}} = F_{\text{P}}\,l_{\text{AB}}$ results in:

$$\begin{aligned} & J_{\text{AC}}\,\ddot{\varphi}_{\text{A}} + c_{\text{A}}\,\varphi_{\text{A}} + c_{\text{CE}}\,\varphi_{\text{A}} - c_{\text{CE}}\,\varphi_{\text{D}} \qquad (10) \\ & + c_{\text{piezo}}\,l_{\text{AB}}^2\sin(\varphi_{\text{A}})\cos(\varphi_{\text{A}}) + \frac{1}{3}\,m_{\text{AC}}\,g\,l_{\text{AC}}\cos(\varphi_{\text{A}}) \\ & - m_{\text{AC}}\,g\,y_{\text{AC}}\sin(\varphi_{\text{A}}) + d_{\text{A}}\,\dot{\varphi}_{\text{A}} + d_{\text{CE}}\,\dot{\varphi}_{\text{A}} - d_{\text{CE}}\,\dot{\varphi}_{\text{D}} = F_{\text{P}}\,l_{\text{AB}} \end{aligned}$$

$$\begin{aligned} & J_{\text{DG}}\,\ddot{\varphi}_{\text{D}} + m_{\text{sensor}}\,l_{\text{DF}}^2\cos^2(\varphi_{\text{D}})\,\ddot{\varphi}_{\text{D}} + c_{\text{D}}\,\varphi_{\text{D}} \\ & + c_{\text{CE}}\,\varphi_{\text{D}} - c_{\text{CE}}\,\varphi_{\text{A}} + \frac{1}{3}\,m_{\text{DG}}\,g\,l_{\text{DG}}\cos(\varphi_{\text{D}}) \qquad (11) \\ & - m_{\text{DG}}\,g\,y_{\text{DG}}\sin(\varphi_{\text{D}}) + m_{\text{sensor}}\,g\,l_{\text{DF}}\cos(\varphi_{\text{D}}) \\ & + d_{\text{D}}\,\dot{\varphi}_{\text{D}} + d_{\text{CE}}\,\dot{\varphi}_{\text{D}} - d_{\text{CE}}\,\dot{\varphi}_{\text{A}} \\ & - m_{\text{sensor}}\,l_{\text{DF}}^2\sin(\varphi_{\text{D}})\cos(\varphi_{\text{D}})\,\dot{\varphi}_{\text{D}}{}^2 = 0 \end{aligned}$$

Under assumption of linear behavior between the force, generated by the piezo F_{P}, and its supplied voltage U_0 the relation:

$$F_{\text{P}} = K_{\text{P}}\,U_0\,, \text{ with } \quad K_{\text{P}} = \frac{\Delta F_{\text{P}}}{\Delta U_0} \qquad (12)$$

results, where signified ΔF_{P} and ΔU_0 are the maximum range of force and voltage, respectively In our case, with

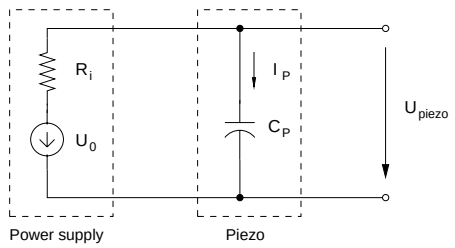

Fig. 10. Electrical model of the piezo, attached to the power supply

a maximum force $F_{\text{P}} = 1800\,\text{N}$ and a maximum voltage of $U_0 = 150\,\text{V}$, the gain K_{P} results to $K_{\text{P}} = 12$.

Electrically, the stack piezo can be modeled in a simplified way as a capacitor with capacitance of C_{P} [46]. Fig. 10 shows the circuit diagram of the piezo attack to the power supply, with the source voltage U_0 and an internal resistance R_i. The voltage applied to the piezo is labeled with U_{piezo} and the current with I_{P}. Using Kirchhoff's law the following equation results:

$$U_0 = U_{piezo} + R_i\,I_{\text{P}}\,, \text{ with } \quad I_{\text{P}} = C_{\text{P}}\,\dot{U}_{piezo}. \qquad (13)$$

Thus, the dynamic behavior of the source voltage U_0 and the piezo voltage U_{piezo} can be described by:

$$\dot{U}_{piezo} = -\frac{U_{piezo}}{R_i\,C_{\text{P}}} + \frac{U_0}{R_i\,C_{\text{P}}}. \qquad (14)$$

For further system analysis and controller design, the dynamic equations of the lever system (10), (11), as well as the electromechanical equations (12), (14) have been transformed in state space form:

$$\dot{\boldsymbol{x}} = \boldsymbol{A}\,\boldsymbol{x} + \boldsymbol{b}\,u + \boldsymbol{z}(\varphi_{\text{D}}, \dot{\varphi}_{\text{D}})\,, \quad y = \boldsymbol{c}^T\,\boldsymbol{x}. \qquad (15)$$

The state vector $\boldsymbol{x}$ and the control input u can be defined to:

$$\boldsymbol{x} = \begin{pmatrix} U_{piezo} \\ \varphi_{\text{A}} \\ \dot{\varphi}_{\text{A}} \\ \varphi_{\text{D}} \\ \dot{\varphi}_{\text{D}} \end{pmatrix}, \quad u = U_0. \qquad (16)$$

Based on this the system matrix $\boldsymbol{A}$, the input vector $\boldsymbol{b}$ and the output vector $\boldsymbol{c}$ calculate to:

$$\boldsymbol{A} = \begin{pmatrix} -\frac{1}{R_i\,C_{\text{P}}} & 0 & 0 & 0 & 0 \\ 0 & 0 & 1 & 0 & 0 \\ \frac{K_{\text{P}}\,l_{\text{AB}}}{J_{\text{AC}}} & \frac{-c_{\text{A}} - c_{\text{CE}} - c_{\text{piezo}}\,l_{\text{AB}}^2 + m_{\text{AC}}\,g\,y_{\text{AC}}}{J_{\text{AC}}} & \frac{-d_{\text{A}} - d_{\text{CE}}}{J_{\text{AC}}} & \frac{c_{\text{CE}}}{J_{\text{AC}}} & \frac{d_{\text{CE}}}{J_{\text{AC}}} \\ 0 & 0 & 0 & 0 & 1 \\ 0 & \frac{d_{\text{CE}}}{J_{\text{DG}} + m_{\text{sensor}}\,l_{\text{DF}}^2} & \frac{c_{\text{CE}}}{J_{\text{DG}} + m_{\text{sensor}}\,l_{\text{DF}}^2} & \frac{-c_{\text{D}} - c_{\text{CE}} + m_{\text{DG}}\,g\,y_{\text{DG}}}{J_{\text{DG}} + m_{\text{sensor}}\,l_{\text{DF}}^2} & \frac{-d_{\text{D}} - d_{\text{CE}}}{J_{\text{DG}} + m_{\text{sensor}}\,l_{\text{DF}}^2} \end{pmatrix}, \qquad (17)$$

$$\boldsymbol{b} = \begin{pmatrix} \frac{1}{R_i\,C_{\text{P}}} \\ 0 \\ 0 \\ 0 \end{pmatrix}, \quad \boldsymbol{c} = \begin{pmatrix} 0 \\ 0 \\ l_{\text{DG}} \\ 0 \end{pmatrix}. \qquad (18)$$

The disturbance vector $\boldsymbol{z}(\varphi_{\mathrm{D}}, \dot{\varphi}_{\mathrm{D}})$ containing constant and nonlinear terms of (11) is:

$$\boldsymbol{z}(\varphi_{\mathrm{D}}, \dot{\varphi}_{\mathrm{D}}) = \begin{pmatrix} 0 \\ \frac{m_{\mathrm{AC}}\, g\, l_{\mathrm{AC}}}{3\, J_{\mathrm{AC}}} \\ 0 \\ -\frac{m_{\mathrm{sensor}}\, l_{\mathrm{DF}}^2 \sin(\varphi_{\mathrm{D}}) \cos(\varphi_{\mathrm{D}})\, \dot{\varphi}_{\mathrm{D}}{}^2 - \frac{1}{3}\, m_{\mathrm{DG}}\, g\, l_{\mathrm{DG}} + m_{\mathrm{sensor}}\, g\, l_{\mathrm{DF}}}{J_{\mathrm{DG}} + m_{\mathrm{sensor}}\, l_{\mathrm{DF}}^2} \end{pmatrix}. \tag{19}$$

On transformation of (10) and (11) into the state space form (15) approximations for small angles:

$$\sin(\varphi) \approx \varphi, \quad \cos(\varphi) \approx 1, \text{ for } \quad \varphi \ll 1. \tag{20}$$

have been made. Because of very small angles of φ_{A} and φ_{D} this is practicable.

Below the parameters of the system matrix $\boldsymbol{A}$ will be specified mathematically. The stiffness coefficients c of the joints A and D, are calculated based on a homogeneously straight bending beam. They can be calculated going out from the deflection curve derived by the hypothesis of Bernoulli:

$$w''(x) = -\frac{M(x)}{EI(x)} = -\frac{M_0}{2EI}\left(1 - \frac{x}{l}\right), \tag{21}$$

where $w''(x)$ is the beam deflection in relation to the distance of his fixation x, M_0 the maximum momentum at the fixation point, E represents the shear modulus of the used steel and I the geometrical momentum of inertia. For the maximum length $x = l$ of deflection line as well as the constraint $w'(0) = 0$ due to no bending at the fixation point, the integration of (21) over the length of the bending beam results in:

$$w'(l) = -\frac{M_0}{EI}\, l. \tag{22}$$

As $w'(l)$ represents the gradient of the beam deflection at its end point the relation to φ is given to:

$$w'(l) = \tan(\varphi) \approx \varphi\,, \text{for} \quad \varphi \ll 1. \tag{23}$$

By inserting the specific values:

$$I = \frac{bh^3}{12}, \tag{24}$$

(23) can be transformed under assumption of a short beam to:

$$M_0(\varphi) = E\,\frac{2\,b\,h^3}{12\,l}\,\varphi. \tag{25}$$

The potential energy of the beam caused by bending can be calculated to, see [47]:

$$E_{pot} = \frac{1}{2}\int_0^{\varphi} M_0(\varphi')\, d\varphi' = \frac{1}{2}\,E\,\frac{b\,h^3}{12\,l}\,\varphi^2 = \frac{1}{2}\,c\,\varphi^2. \tag{26}$$

Hence the stiffness of the bending beams in relation to the geometrical form and the modulus of elasticity E results to:

$$c = E\,\frac{b\,h^3}{12\,l^3}. \tag{27}$$

Tab. IV displays the the stiffness of the three bending joints, with $E = 210000\,\frac{\mathrm{N}}{\mathrm{mm}^2}$. As listed in Tab. III, the stiffness coefficient of the stack piezo is given by $c_{piezo} = 60000\,\frac{\mathrm{N}}{\mathrm{mm}^2}$.

TABLE IV
STIFFNESS COEFFICIENTS

Joint	b [mm]	h [mm]	l [mm]	c [Nm]
A	2.5	0.6	4	2.363
B	2.5	0.5	2.9	1.886
CE	2.5	0.5	2.9	1.886

The inertia of the lower and upper level could be computed directly by the CAD program based on the geometrical data and the density of the used steel to:

$$J_{\mathrm{AC}} = 17.92 \cdot 10^{-7}\,\mathrm{kg\ m}^2, \quad J_{\mathrm{DG}} = 57.64 \cdot 10^{-7}\,\mathrm{kg\ m}^2 \tag{28}$$

Additional values, that are important to compute the system matrix and vectors, are summarized in Tab. V

With these results, the coefficients of the state space system (15) can be calculated, except for the damping values $d_{\mathrm{A}}, d_{\mathrm{CE}}, d_{\mathrm{D}}$. In a first approach these damping values have been reduced to one unknown damping value D, based on the geometrical coherences of the bending beams. This damping values D can be defined in the following validation of the calculated dynamic model.

To use the calculated dynamic system for the further controller design, it has been validated with the real hardware setup. Initially the frequency response of the hardware system has to be compared to the computed model.

Fig. 14 shows the open loop frequency response characteristics of the real system in within a range of $10\,\mathrm{Hz} - 10\,\mathrm{kHz}$, caused by a swept sine signal and processed by a wave analyzer. The first resonance frequency of the system can be identified clearly at the frequency of $88\,\mathrm{Hz}$. After this resonance magnification, the amplification of the system falls significantly with a rate of $40\,\mathrm{dB}$ per decade. A second resonance magnification can be seen at the frequency of approx. $2.8\,\mathrm{kHz}$. The behavior in the upper frequency range ($> 400\,\mathrm{Hz}$) deviates from the expected characteristics of the modeled PDT_5-System, probable caused by the nonlinearities summarized in the disturbance term of the state space model (19). In comparison thereto the calculated dynamic model deviates with its resonance frequency of $110\,\mathrm{Hz}$ by about 20% from the real setup. The second frequency magnification differs by about 13%. This deviation has been adjusted by tuning the coefficients of the modeled system.

Due to the fact, that our mathematical model consists of a PDT_5-System, the damping value D must be identified at the hardware setup. Therefore the captured step response of the real system has been used to adapt the damping behavior of the calculated model by tuning the damping value D in an iteration loop. Finally, the coefficients of the system matrix $\boldsymbol{A}$ in (18), for the state space system

TABLE V

DEVIATIONS AND MASSES OF THE COMBINED LEVER SYSTEM

1st lever	2nd lever	Sensor	Piezo
$l_{\text{AC}} = 33\,\text{mm}$	$l_{\text{DG}} = 72\,\text{mm}$	$l_{\text{DF}} = 51\,\text{mm}$	$l_{\text{AB}} = 3.5\,\text{mm}$
$m_{\text{AC}} = 3.862\,\text{g}$	$m_{\text{DG}} = 6.381\,\text{g}$	$m_{sensor} = 0.65\,\text{g}$	–
$y_{\text{AC}} = 10\,\text{mm}$	$y_{\text{DG}} = 5.9\,\text{mm}$	–	–

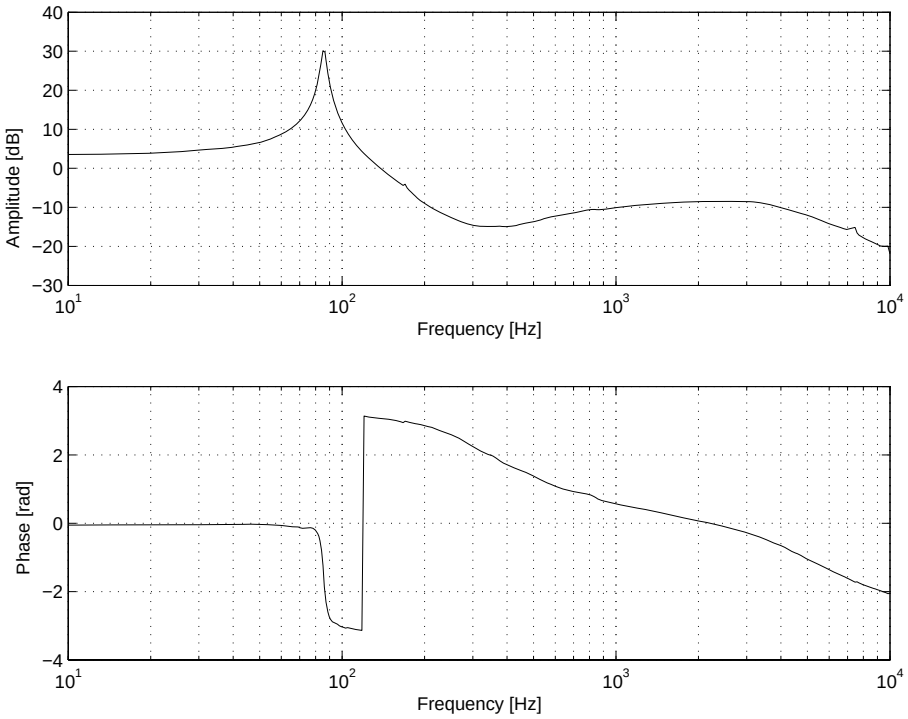

Fig. 11. Open loop frequency response, measured by experiment

(15) results to:

$$\boldsymbol{A} = \begin{pmatrix} -7936 & 0 & 0 & 0 & 0 \\ 0 & 0 & 1 & 0 & 0 \\ 4.946 \cdot 10^8 & -2.476 \cdot 10^8 & -100 & 5.7 \cdot 10^5 & 24 \\ 0 & 0 & 0 & 0 & 1 \\ 0 & 1.425 \cdot 10^5 & 6.25 & -2.85 \cdot 10^5 & -12 \end{pmatrix} \tag{29}$$

Fig. 12 shows the step response at a range of $150\,\mu$m to $750\,\mu$m of the real setup in comparison with the computed dynamic model. Thereby the computed model follows the real system with a small phase shift. Also the decay of the amplitude is not exactly as fast as at the real system. But is clear that the characteristic of the real system is sufficiently approximated by the computed model, making it a solid basis for further control design.

Control concept

Based on the dynamic model of the combined lever system, in this section the concept and parametrization of the controller is described.

Fig. 13 shows the overall control concept of the low frequency module. The input value (w) contains the set-point of position that is followed by the pin, measured at the endpoint of the lever system (y). Basically, the entire control structure can be divided in two control loops:

- An **output control** loop at the outer control structure is to guaranty steady state control accuracy. It consists of an integral action controller, that ensures a good reference tracking of the control loop.
- The **state control** in the inner control loop is implemented to enhance the dynamic behavior of the plant. It is realized by an observer based control structure.

Below both control loops are described separately, starting with the outer control loop.

Outer control loop: The integral action controller for the outer control loop has been designed by an LQ-control approach [48]. Therefore the equation of the dynamic system in state space form (15) has been extended by an

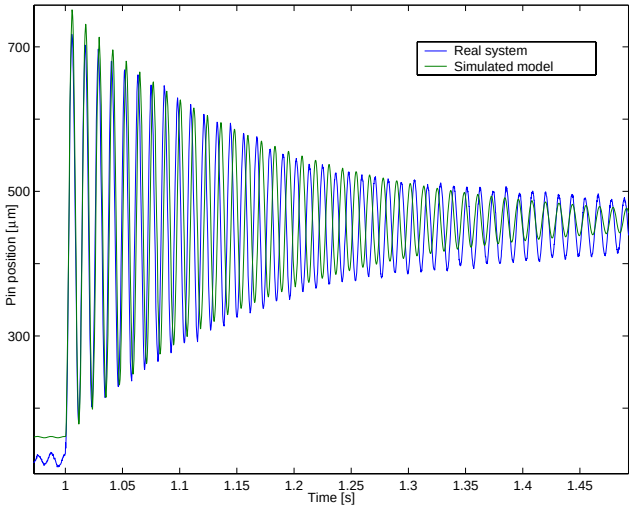

Fig. 12. Step response of the real system compared to the model.

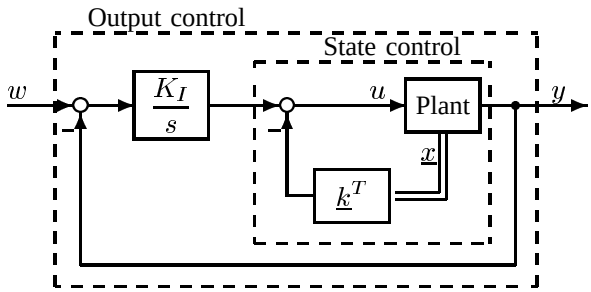

Fig. 13. Control structure

integrator to:

$$\begin{pmatrix} \dot{\boldsymbol{x}} \\ \dot{x}_I \end{pmatrix} = \begin{pmatrix} \boldsymbol{A} & 0 \\ -\boldsymbol{c}^T & 0 \end{pmatrix} \begin{pmatrix} \boldsymbol{x} \\ x_I \end{pmatrix} + \begin{pmatrix} \boldsymbol{b} \\ 0 \end{pmatrix} u + \begin{pmatrix} \boldsymbol{0} \\ 1 \end{pmatrix} w, \tag{30}$$

with the input value w and the matrix and vectors displayed in (18). In the closed loop the regulation value has been built by the states of the system to:

$$u = -\boldsymbol{k}^T \begin{pmatrix} \boldsymbol{x} \\ x_I \end{pmatrix}, \text{with} \quad \boldsymbol{k}^T = (k_1\ k_2\ k_3\ k_4\ k_5\ k_I). \tag{31}$$

The coefficients of the gain vector $\boldsymbol{k}$ have been found by solving the optimization problem:

$$\min_{\boldsymbol{k}} J(\boldsymbol{x}, u, \sigma) = \int_0^\infty e^{2\sigma t}[\boldsymbol{x}^T(t)\boldsymbol{Q}\boldsymbol{x}(t) + u^2(t)r]\, dt,$$
$$\text{with} \quad Re(\lambda_i) < -\sigma, \tag{32}$$

where the matrix $\boldsymbol{Q}$ weights the states $\boldsymbol{x}$ of the system and the coefficient r weights the control input u. With the stability margin σ, the settling time can be determined. To prevent the control input from saturation of the maximum supply voltage of the stack piezo (150 V) the control input weight coefficient is set to $r = 1 \cdot 10^6$, whereas the weighting matrix of the states is set to $\boldsymbol{Q} = \text{diag}(1)$.

The standardized step response in Fig. 14 shows the result of the LQ-controller design at the reference input regarding different stability margins. In every case the

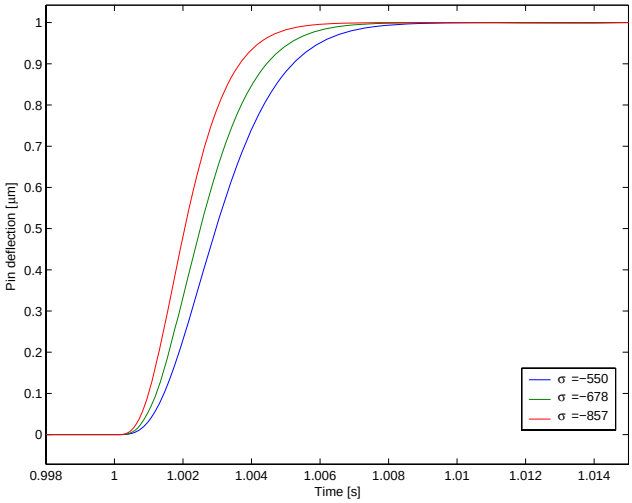

Fig. 14. Standardized step response at different stability margins

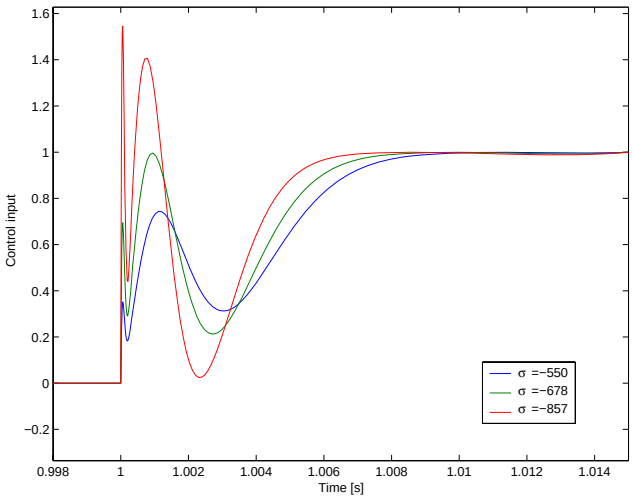

Fig. 15. Standardized control input at different stability margins

signal has aperiodic response behavior. Fig. 15 displays the standardized characteristics of the control input during the step response in terms of the maximum set voltage of 150 V. It can be seen, that stability margins lower than $\sigma < -678$ bring the control input in saturation of the stack piezo amplifier. For further calculations a stability margin of $\sigma = -678$ has been chosen. With this value we get an step response time of $t = 7$ ms and the gain coefficients result to:

$$\begin{pmatrix} \boldsymbol{k} \\ k_I \end{pmatrix} = \begin{pmatrix} 10,676 \\ -0,64 \\ 1,0715 \cdot 10^{-3} \\ 62,473 \\ 0,074536 \\ 26439 \end{pmatrix} \tag{33}$$

Inner control loop: To enhance the dynamic behavior of the plant and compensate the noise of the position sensor, the inner control loop has been designed as a proportional state controller. Therefore the states of the computed mechanical system have been recovered from

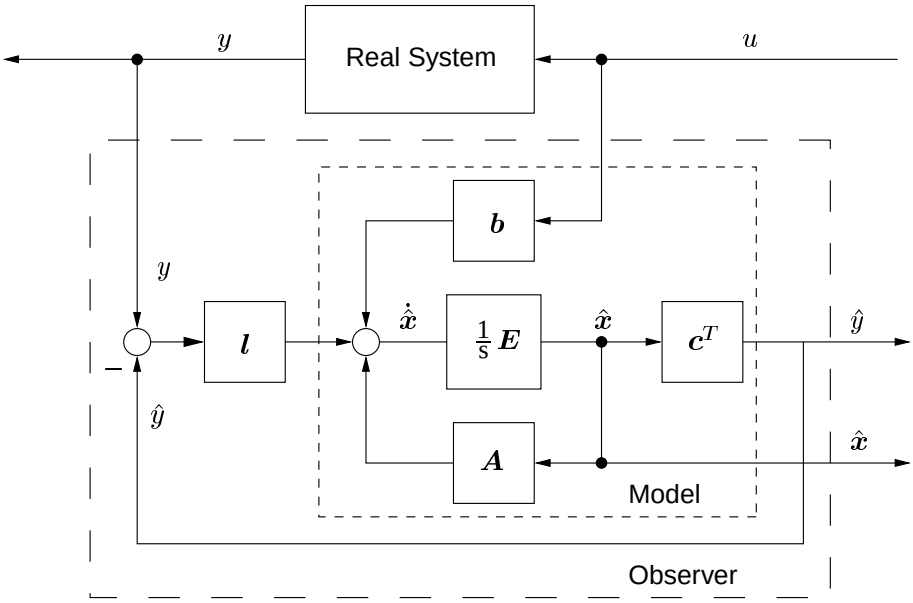

Fig. 16. Kalman-Bucy-Filter block diagram [49]

the measured position signal. This has been realized with a *Kalman-Bucy-Filter*, schematically shown in Fig. 16. It consists of a parallel observer system ($\hat{\boldsymbol{A}}, \hat{\boldsymbol{b}}$), based on the computed state space model, with the control input and the by the vector $\boldsymbol{l}$ weighted difference of the measured respective computed output $(y, \hat{y})$ of the plants as input value. So, the estimated states of the system are given by the state vector $\hat{\boldsymbol{x}}$. Under assumption of compliance between the real plant and the computed model ($\hat{\boldsymbol{A}} = \boldsymbol{A}$, $\hat{\boldsymbol{b}} = \boldsymbol{b}$, and $\hat{\boldsymbol{c}} = \boldsymbol{c}$) the state space form of the observer results to:

$$\dot{\hat{\boldsymbol{x}}} = (\boldsymbol{A} - \boldsymbol{l}\boldsymbol{c}^T)\hat{\boldsymbol{x}} + \boldsymbol{b}u + \boldsymbol{l}y. \tag{34}$$

The Kalman gain vector $\boldsymbol{l}$ has been determined on minimization of the performance index of the state vector error $\tilde{\boldsymbol{x}}(t) = \hat{\boldsymbol{x}}(t) - \boldsymbol{x}(t)$ between the observer (34) and the system model (15) by minimization of variance:

$$\begin{aligned} J[\tilde{\boldsymbol{x}}(t)] &= E\left[||\tilde{\boldsymbol{x}}(t)||^2\right] \qquad (35) \\ &= \lim_{T\to\infty} \frac{1}{2T} \int_{-T}^{+T} ||\tilde{\boldsymbol{x}}(t)||^2 \, dt \longrightarrow \min. \end{aligned}$$

With the equation for the Kalman gain $\boldsymbol{l}$:

$$\boldsymbol{l} = \Pi_+ \boldsymbol{c} w^{-1} \,. \tag{36}$$

The covariance matrix Π_+ consists of the positive definite solution as a result of solving the *Matrix-Riccati-Equation*:

$$-\boldsymbol{A}\Pi - \Pi\boldsymbol{A}^T + \Pi\boldsymbol{c}w^{-1}\boldsymbol{c}^T\Pi - \boldsymbol{V} = 0 \tag{37}$$

The weighting matrix $\boldsymbol{V}$ is determined by the process noise, whereas the weighting value w depends on the measurement noise. They are specified by measurements on the real system in an iterative process to: $\boldsymbol{V} = \mathrm{diag}(10^{-4}), w = 1.2 \cdot 10^{-7}$. The Kalman gain vector $\boldsymbol{l}$ results to:

$$\boldsymbol{l} = \begin{pmatrix} 3546,2 \\ -52643 \\ -1,304 \cdot 10^9 \\ 5176,8 \\ 1,34 \cdot 10^7 \end{pmatrix} \tag{38}$$

Controller performance

The entire dynamic system of the low frequency actuator containing an output control loop at the outer and a Kalman-Bucy-Filter at the inner control loop can be summarized in state space form as:

$$\begin{pmatrix} \dot{\boldsymbol{x}} \\ \dot{x_I} \\ \dot{\hat{\boldsymbol{x}}} \end{pmatrix} = \begin{pmatrix} \boldsymbol{A} & k_I\boldsymbol{b} & -\boldsymbol{b}\,\boldsymbol{k}^T \\ 0 & 0 & -\boldsymbol{c}^T \\ \boldsymbol{l}\,\boldsymbol{c}^T & 0 & \boldsymbol{A} - \boldsymbol{l}\,\boldsymbol{c}^T \end{pmatrix} \begin{pmatrix} \boldsymbol{x} \\ x_I \\ \hat{\boldsymbol{x}} \end{pmatrix} + \begin{pmatrix} 0 \\ 0 \\ \boldsymbol{b} \end{pmatrix} u + \begin{pmatrix} 0 \\ 1 \\ 0 \end{pmatrix} w \tag{39}$$

Due to the fact of using the LQ-control approach in both cases for controller design, the entire controller for the low frequency module is inherently stable. For measuring the performance of the entire controller, a step response in both directions of the pin moving space has been performed.

Fig. 17 shows the measured pin position of a step response from $1100\,\mu$m down to $250\,\mu$m, as well as the pin position, calculated by the observer. After a small overshot, the system reaches a nearly steady state after approximately 20 ms. In Fig. 18 the corresponding characteristic of the control voltage for the stack piezo amplifier is shown. Thereby, proportional amplification coefficient of the stack piezo amplifier amounts to 15.

The measured observer pin position on a step response from $250\,\mu$m up to $1100\,\mu$m is shown in Fig. 19. Compared with the step downward it has a longer setting time supposed by the countering influence of inertia. Other reasons

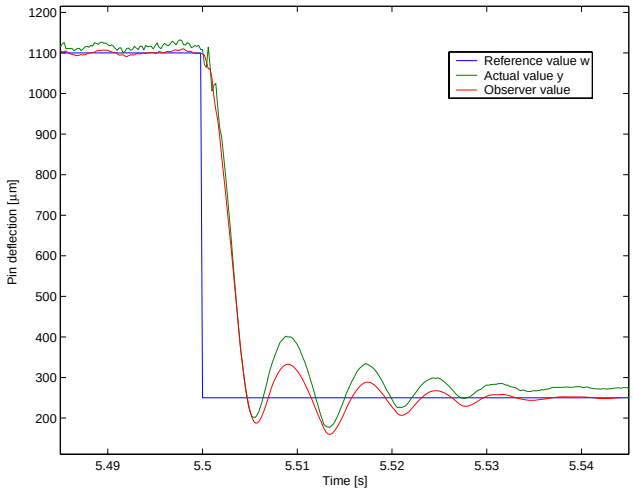

Fig. 17. Closed loop step response from 1100 μm to 250 μm

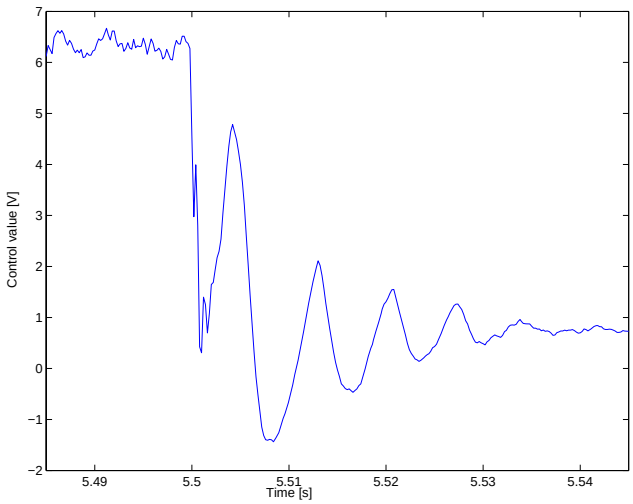

Fig. 18. Control input at a step from 1100 μm to 250 μm

could be the neglected nonlinearities. The corresponding control voltage is shown in Fig. 20.

Compared with the open loop step response in Fig. 12 a clear improvement of the positioning accuracy has been reached. Even if the specifications are not reached completely, the resulting low frequency actuator represents a promising approach in actuator technology for tactile pin actuators. Fig. 21 shows the entire hardware setup of the low frequency actuator with position sensor.

C. High frequency module

The high frequency module provides the frequency range above 70 Hz of stimulation in the combined actuator concept. The specifications therefore are: pin excursions up to 20 μm at frequencies up to 1 kHz. These efforts can be realized by a standard stack piezo actuator.

Caused by their functional principle, piezo crystals show a nonlinear behavior in response characteristic e.g. hysteresis of movement [50]. Due to this fact a control design is necessary, to compensate this effects and provide good position accuracy.

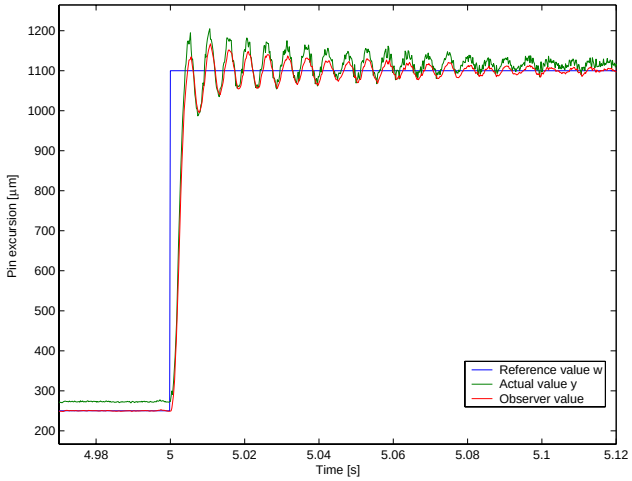

Fig. 19. Closed loop step response from 250 μm to 1100 μm

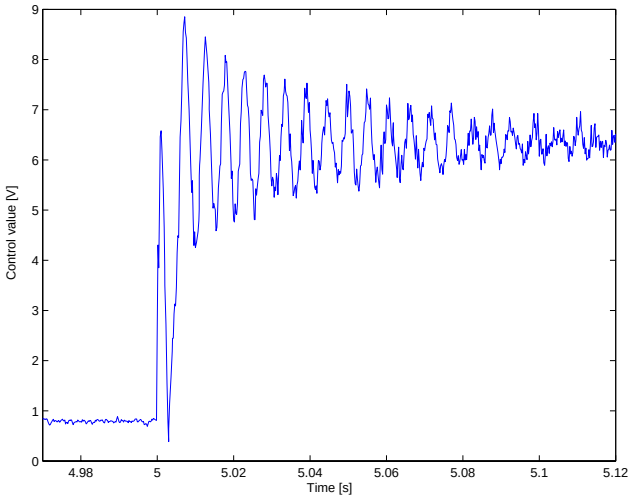

Fig. 20. Control input at a step from 250 μm to 1100 μm

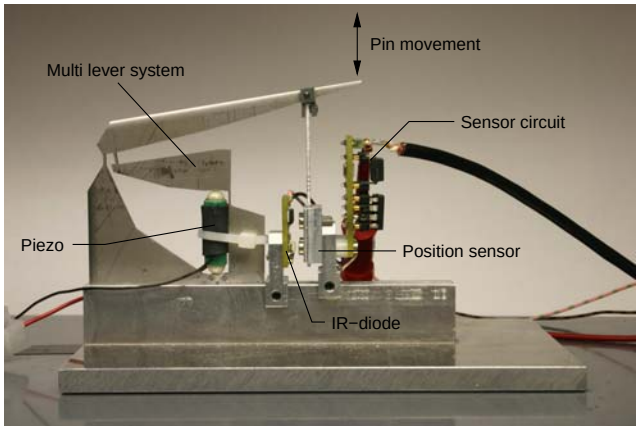

Fig. 21. Complete setup of the low frequency module

For the high frequency module an off-the-shelf stack piezo with an integrated position sensor has been used. A picture of this piezo is shown in Fig. 22 besides the technical data in Tab. VI. Furthermore, the piezo comes pre-pressed. This is necessary to prevent the piezo from

TABLE VI

STACK PIEZO DATA

Type	PSt 150/5/40
Max. stroke	$55\,\mu$m
Max. force	800 N
Prestress	150 N
Stiffness	$12\,\frac{\mathrm{N}}{\mu\mathrm{m}}$
Resonance freq.	20 kHz
Supply voltage	$-30-150$ V
El. capacity	1600 nF
Pos. sensitivity	0.05 nm
Length (L)	46 mm

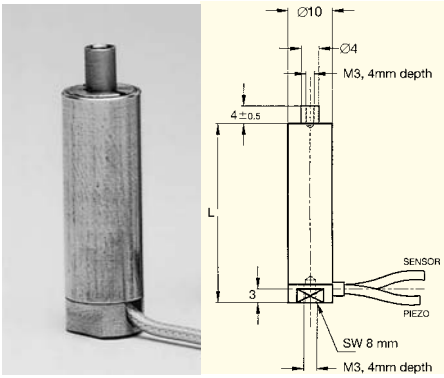

Fig. 22. High frequency stack piezo actuator

destruction caused by unloaded excursion. The range of motion is $55\,\mu$m, thus, in combination with the low frequency module it can be used directly as a part of the whole pin actuator.

The integrated position sensor is based on strain gages attached to the piezo stack. Electrically they build a Wheatstone bridge circuit of resistors. To adapt the movement caused by resistor changing at the bridge circuit, a high impedance amplifier has been built.

Position control

Due to the fact of capacitive behavior of the piezo supplied by a power supply with internal resistance, shown in Fig. 10 the plant can be modeled as a PT_1 – System (first order lag), with the transfer function:

$$F(s) = \frac{\text{excursion}}{\text{supplied voltage}} = \frac{y}{U_0} = \frac{k_g\, k_{piezo}}{1+sT}, \qquad (40)$$

with the voltage gain of the amplifier k_g, and the excursion in relation to the max. input voltage k_{piezo}. The time constant can be determined from the piezo capacity C_{piezo} and the internal resistance of the power supply R_i to $T = R_i C_{piezo}$. As control concept a proportional plus integral controller has been chosen.

Fig. 23 shows the control structure of the high frequency module, with the assumption of an ideal sensor ($F_s = 1$) and the controller coefficients k_I and k_P. For the demanded frequency range of up to 1 kHz a setting time of $T_{set} =$ 1 ms is necessary. Thus, a stability margin of $\sigma_g = -3000$ results. Based on the root locus of the control system and adjustment of the zero point, with repect to the stability margins constraints the control gains have been appointed to: $k_P = 0.3368$ and $k_I = 3200$.

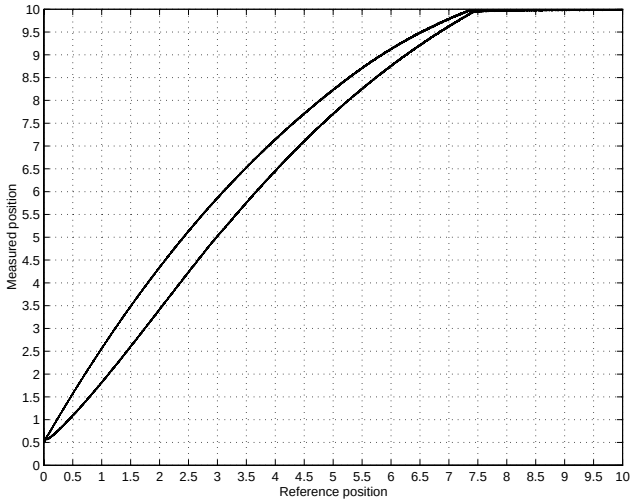

Fig. 24. Hysteresis of the stack piezo

Controller performance: Fig. 24 shows the behavior of the stack piezo in its entire range of movement, where the characteristic hysteresis can be seen.

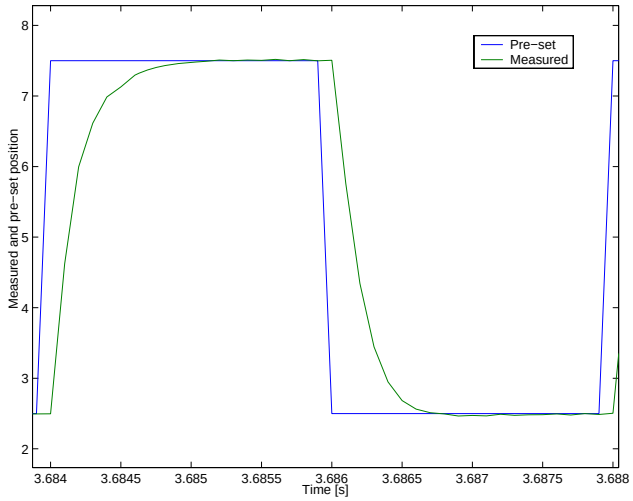

Fig. 25. Pulse signal response at 250 Hz

The results of the position controlled stack piezo, using a PI-control algorithm, are displayed in Fig. 25 and Fig. 26. They show the sinus and pulse response at the same frequency (250 Hz). Thereby, the measured voltage in the range of 0 to 10 V is proportional to the pin excursion of 0 to $40\,\mu$m. In comparison with measurements of the real system the computed model differ in terms of bandwidth with $f_{max} = 950$ Hz of about 10%. However, the controlled high frequency actuator can be used as part of the multi actuated pin concept, as planned.

V. TACTILE SHEAR FORCE PROTOTYPE DEVICE

This section presents the prototype of a shear force display for the finger tip and a first psychophysical evaluation. As seen in chapter III most tactile displays are

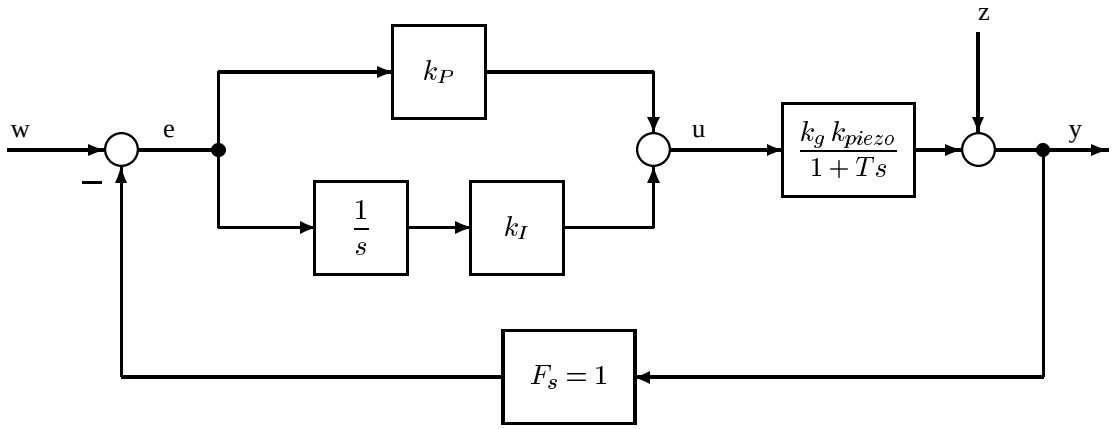

Fig. 23. High frequency module control structure

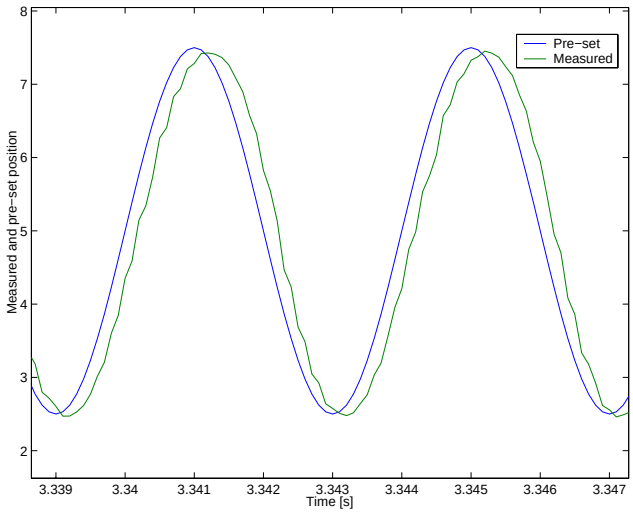

Fig. 26. Sinus wave response at 250 Hz

designed with the aim to display tactile pictures, using pins (needles) arranged in a grid like arrangement, where the pins are movable independently, mostly variably adjustable in position, normal to the surface of the skin. However, from the psychophysical point of view the mechanism of tactile perception is considerably more complex and partly unexplored. At this reason we build a prototype of tactile display, to explore some open questions regarding the tactile shear force perception, whose findings vice versa enhance the development of shear force displays in further design loops.

For the first prototype, presented in this paper, the design is based on the known psychophysical findings and thresholds summarized in chapter II. In order to explore whether the stimuli produced by the display are appropriate for human perception we studied discrimination performance of humans for distinguishing between different directions of pin movement. In a second step we explored the perceptual integration of multi-pin movements.

A. *Technical realization of shear force display*

The fundamental concept of the display is based on a quadratically arranged 2×2 pin array. To exert shear force to the area of the finger tip, each pin is movable laterally to the skin. Thereby it is possible to move each pin independently along both axes of their two-dimensional horizontal directions. Design parameters have been chosen based on psychophysical thresholds. A pin diameter of 1 mm, a center-to-center pin spacing of 3 mm (zero position of lateral movement) and a lateral movement of 2 mm along each axis and for each pin are realized [51].

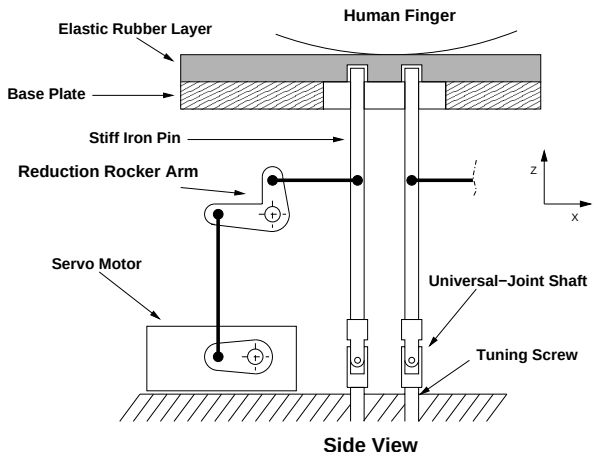

Fig. 27. Mechanical design of shear force display.

The mechanical design for one pin in one axis is schematically shown in Fig. 27. The four pins are in direct contact with the finger tip (optional filtered by an elastic rubber layer). Two rods orthogonal attached to the upper region of each pin transmit two-dimensional movement of the pins. To allow for this movement the four pin bodies are attached with universal-joint shafts that are screwed to the ground plate of the chassis. Tuning screws between the base plate and the joints enable a justification along the z-axis in a small range to vary the indentation offset normal to the finger pulp. The rods are connected over reduction rocker arms to the servo motor levers. To reduce

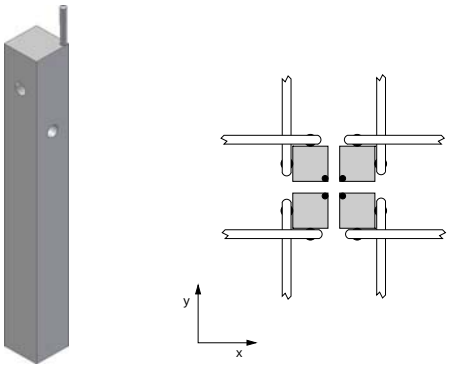

Fig. 28. Pin-body design and arrangement

pin motion normal to the skin down to a tolerable value, the length of the pin raised to 69 mm. In case of a pin diameter of 1 mm a realization of a pin with this dimensions would be unusable because of bending. Furthermore it would be difficult to to attach the two steering rods providing the tangential motion. To avoid this problem, the length of the pin has been reduced to 6 mm and attached to a prismatic body (Fig. 28 left). The right picture of Fig. 28 shows the top view of the mechanical design. The pins are fitted to the inner edge of the bodies (black points) to provide a large motion workspace for the pins.

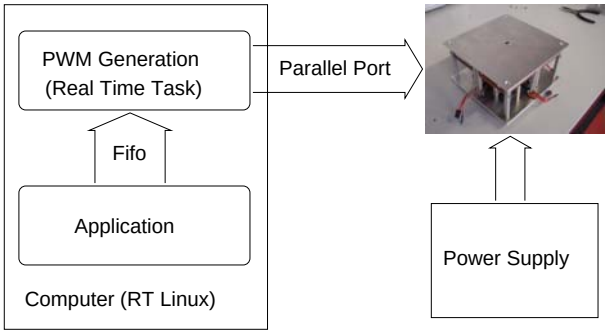

Fig. 29. Control system.

On the actuator side, we use of-the-shelf servo motors, selected on criteria like high performance, small deviations, and light weight. The servo motors come with a position control circuit, accessed by a pulse-width modulated signal, which contains the commanded position information. Fig. 29 shows the schematic design of the computer interface. A real-time task generates the required signals for the eight servo motors at the printer-port of the computer, whose data lines are connected to the corresponding servo motors. In the application process the position information for the servo motors are calculated and communicated to the real-time task. To provide sufficient power for the servo motors an external power supply is used.

The upper picture in Fig. 30 shows the display in use with a close-up view of the pin area that is in contact with the finger tip through a hole in the cover plate. A more detailed view in the lower picture of Fig. 30 shows the mechanical details of the display like the pin bodies, the control rods, and the servo motors. Tab. V-A summarizes the technical data of the tactile shear force display.

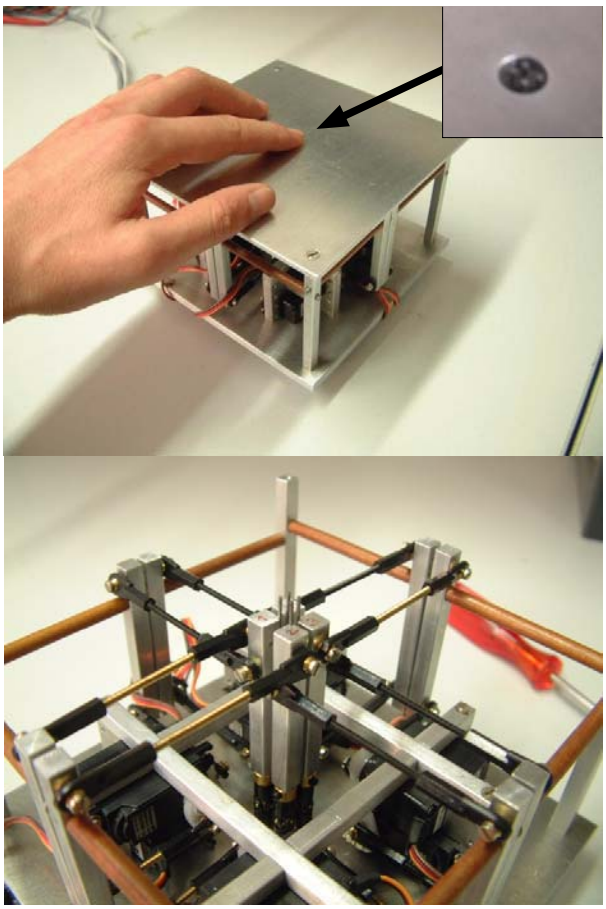

Fig. 30. Hardware setup of the shear force display.

TABLE VII
TECHNICAL DATA OF THE SHEAR FORCE DISPLAY.

Property	Value
Positioning resolution	$10\,\mu$m
Max. pin force (per axis)	4.23 N
Max. pin velocity	22.8 mm/s
Pin work space	2×2 mm
Size	$150 \times 150 \times 90$ mm
Weight	1100 g

B. Psychophysical evaluation

The psychophysical evaluation focused on the question of whether the stimuli produced by the display are appropriate for human perception. In Experiment 1 we studied discrimination performance for different directions of single-pin movement. To our knowledge there is just a single study on human direction discrimination on the finger tip [53]. That study, however, investigated single pin movement paths of a length that our multi-pin device has not been designed to display. In the second experiment, we studied integration of parallel movement of multiple pins. From well-established theories on sensory integration in humans, we expected that discrimination performance should profit from multi- as compared to single-pin display

- at least if the brain processes movements displayed by the single pins independently from another [13].

Experiment 1

Methods. 14 right-handed participants (9 females, age range 21 to 40 years, average age 26) took part for pay. None of them had any known tactile deficit. The participants sat in a quiet room in front of a table with their left elbow resting comfortably on a custom-made support. By using robust tape their left hand was attached to the shear force display so that the the tip of their left index finger was reliably centered at the midpoint of the pin display. We used the shear force display with a single pin only (for this experiment the other three pins were removed) and a particular base plate (Fig. 31 right, upper) that allowed for individual adaptation of gap size and, thus, maximal spread of skin stretch. A blind prevented participants from seeing the display and white noise displayed via headphones masked the sounds of the display during pin movement. A custom-made program on a PC controlled the stimulus presentation and collected the responses.

Tactile stimuli were unidirectional single strokes of $1\,\mathrm{mm}$ length (velocity $1\,\mathrm{cm/s}$) starting at the midpoint of the display. For the strokes we defined eight standard directions with respect to the finger (separated by $45°$, Fig. 31 left). To each standard a set of 19 comparison strokes was chosen, the directions of which were distributed in $10°$ steps around the corresponding standard within an area of $\pm 90°$ (Fig. 31 right, lower).

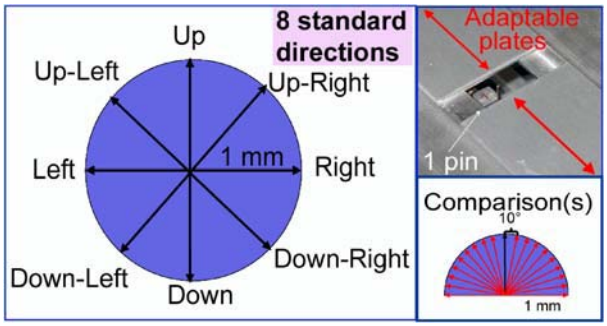

Fig. 31. Setup in Experiment 1.

In each single trial the participants successively felt a standard and a comparison stroke and, then, had to decide by a button press which of the two strokes had been oriented more in clock-wise direction. Between the strokes participants had to lift their finger to allow for moving the pin back to the midpoint without evoking tactile stimulation. Required finger movements were signaled by different sounds on the headphones.

Each pair of standard and comparison stroke was presented twelve times during the experiment. The order of standard and comparison was balanced across repetitions. The order of pairs was completely random. For each single participant the experiment lasted about four hours performed within two sessions (including three breaks) on different days.

Using the psignifit toolbox for Matlab [54] we fitted individual psychometric functions (cumulative Gaussians; Maximum Likelihood procedure) to the proportion of trials in which the comparison stroke was perceived as more clockwise-oriented than the standard stroke - against the comparison direction. From the fits, we obtained individual 84%-discrimination thresholds per standard.

Results and Discussion. After the experiment all participants reported that they had felt pin translation and most that they had perceived also skin stretch. Figure 32 depicts medians and quartiles of the individual discrimination thresholds by standard direction. Median thresholds ranged from $23°$ to $35°$, thresholds quartiles ranged from a maximal 75%-percentile of $54°$ down to a minimal 25% -percentile of $12°$. Further, the individual thresholds per standard direction entered a Friedman test. The test reached significance, $\chi^2(7) = 20.7, p < .01$, indicating a perceptual anisotropy, i.e., participants discriminated better between movements in up-direction as compared to the other directions.

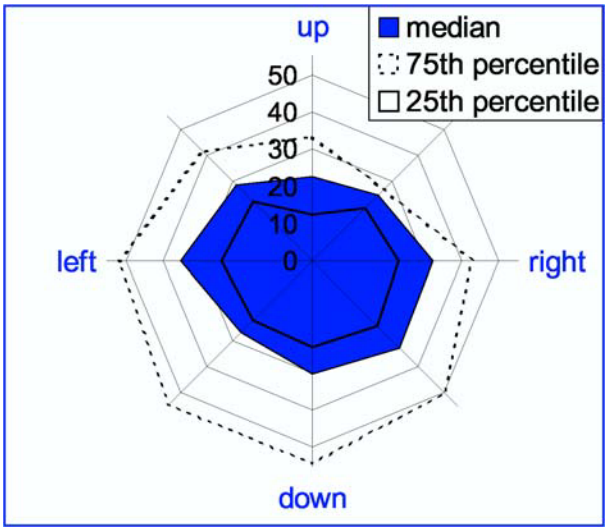

Fig. 32. Medians and quartiles of 84%-thresholds by standard direction.

Most importantly here, threshold magnitudes demonstrate that humans can well discriminate between the directions of the movements displayed. It is also important to note that the technical directional resolution of the shear force device clearly exceeds the perceptual thresholds we observed. Thus, the shear force display produces tactile stimuli that are appropriate for human perception, and shear forces seem to be usable to obtain a differentiated impression of at least one environmental aspect. Consequently, the next experiment explored to what degree shear forces displayed by more than one pin are integrated.

Experiment 2

Methods. Twelve paid right-handed participants without known tactile deficits took part in Experiment 2 (6 females, age range 19 to 40 years, average age 27). The same setup, procedure and stimuli as in Experiment 1 were used.

However, we defined just two standard directions with respect to the finger (up and down) including 19 corresponding comparison directions. Directions were displayed either with one, two or four pins (other pins removed, cf. Fig. 33 for directions and pin configuration). In the multi-pin conditions all pins moved simultaneously and with identical velocity and direction; the pins were separated by 3 mm (center-to-center). Trials with one, two or four pins were performed in three sessions on different days. The order of sessions was balanced between participants according to a Latin square design. The whole experiment lasted about three hours.

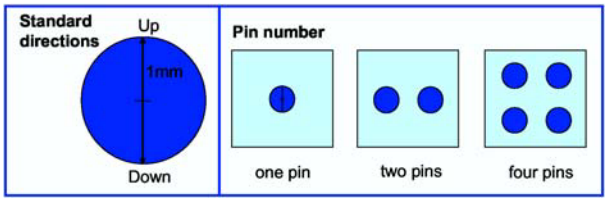

Fig. 33. Setup in Experiment 2.

Results and Discussion. Fig. 34 depicts medians and quartiles of the individual discrimination thresholds by standard direction and pin number. Median thresholds ranged from $19°$ to $23°$, thresholds quartiles ranged from a maximal 75%-percentile of $33°$ down to a minimal 25%-percentile of $16°$. The individual thresholds per standard direction and pin number entered a Friedman test. The test clearly failed to reached significance, $\chi^2(5) = 6.7$, $p > .20$, demonstrating that in this experiment participants' discrimination performance did neither differ between the two movement directions nor between the conditions with different pin numbers.

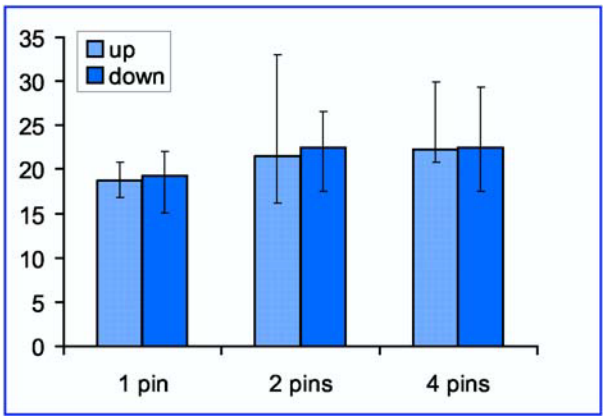

Fig. 34. Medians and quartiles of 84%-thresholds by standard direction and pin number.

In general, the magnitude of discrimination thresholds in Experiment 2 confirmed that humans well discriminate between the directions of the movements displayed and that the perceptual resolution did not exceed the technical resolution. Thresholds in this experiment tended to be slightly lower than in Experiment 1. There were, however, substantially less different standard directions in this as compared to the last experiment, so that memory effects may have played a role. Surprisingly, we were not able to replicate the advantage of up-directions observed in Experiment 1. Most importantly, we did not find any effect of pin number on discrimination performance. According to well-established models on human signal integration, the human brain integrates independent redundant signals on the same physical property such that the integrated signal is more reliable than the single signals were [13]. The lack of an integration benefit in the present study may indicate that the movements of the different pins of the shear force device were not independently processed in the perceptual system.

VI. Conclusion

A. Combined pin actuator

Regarding our research on advancement in actuator technologies, the FEM based design of a cascaded two lever mechanical structure for a multi actuated tactile pin actuator is presented. The lever system forms the low frequency module of the combined pin actuator and reach an excursion length of 1.7 mm. The position control concept of the module is based on position measurement and full state feedback control using the 5-dimensional state vector of the linear time invariant model. State feedback gains are designed using a linear quadratic regulator approach, the state is estimated from position measurements using a Kalman filter approach. Experimental results confirm that the linear model of the system is very close to the hardware prototype. The control approach shows good performance in position control, which is validated with experimental results of the prototype hardware. The high frequency module consists of an of-the-shelf piezo crystal providing large bandwidth, but only for small excursions. Experimental results confirm the effectiveness of this second actuator in the high frequency module of the multi actuated pin. Both modules apart have the expected functionality and good performance. In further steps they will be mechanically combined in a serial manner.

B. Tactile shear force prototype device

This paper presents the design and buildup of a novel tactile shear force display. In the experiments we analyzed whether the shear force display produces tactile stimuli that are appropriate for human perception. Both experiments demonstrated that humans can well discriminate between the shear forces displayed, and also that their perceptual resolution does not exceed the already realized technical resolution of the device. Further development of the device can take advantage of these facts. In Experiment 2 we further found evidence that the human brain does not process stimulation from different pins independent of another at least concerning movement direction. On the one hand, future evaluation of the present prototype will have to explore to what degree non-simultaneous, differential multi-pin patterns of movement are able to evoke discriminable percepts. On the other hand, future

development of the shear force display will have to include mechanisms that allow for an increased pin distance.

ACKNOWLEDGMENTS

This work is part of the TOUCH-HapSys project financially supported by the 5th Framework IST Programme of the European Union, action line IST-2002-6.1.1, contract number IST-2002-38040. For the content of this paper the authors are solely responsible for, it does not necessarily represent the opinion of the European Community.

REFERENCES

[1] R. Howe, W. Peine, D. Kantarinis, and J. Son, "Remote palpation technology," *Engineering in Medicine and Biology Magazine*, vol. 14, pp. 318 – 323, 1995.

[2] P. Kammermeier, M. Buss, and G. Schmidt, "Actuator array for display of distributed tactile information - design and preliminary experiments," in *Proceedings of the ASME Dynamic Systems and Control Division*, vol. 2, 2000, pp. 1315–1321.

[3] M. Shinohara, Y. Shimizu, and A. Mochizuki, "Three-dimensional tactile display for the blind," in *Rehabilitation Engineering, IEEE Transactions on*. IEEE, 1998, vol. 6, pp. 249 – 256.

[4] J.-H. Lee, I.-S. Ahn, and J.-O. Park, "Design and implementation of tactile feedback device using electromagnetic type," in *Intelligent Robots and Systems, 1999. IROS '99*, vol. 3, 1999, pp. 1549 – 1554.

[5] Y. Ikei, K. Wakamatsu, and S. Fukuda, "Texture presentation by vibratory tactile display-image based presentation of a tactile texture," in *Virtual Reality Annual International Symposium, 1997*, 1997, pp. 199 – 205.

[6] Y. Ikei, "TextureExplorer: A tactile and force display for virtual textures," in *HAPTICS'02*. IEEE, 2002.

[7] I. Summers, C. Chanter, A. Southall, and A. Brady, "Results from a tactile array on the fingertip," in *EuroHaptics*, 2001, `http://www.eurohaptics.net`.

[8] M. Konyo, S. Tadokoro, and T. Takamori, "Artificial tactile feel display using soft gel actuators," in *Int. Conference an Robotics & Automation*, 2000, pp. 3416–3421.

[9] M. Konyo, K. Akazawa, S. Tadokoro, and T. Takamori, "Tactile feel display for virtual active touch," in *Intelligent Robots and Systems, 2003. (IROS 2003)*, vol. 3, 2003, pp. 3744 – 3750.

[10] M. Salada, J. Colgate, M. Lee, and P. Vishton, "Validating a novel approach to rendering fingertip contact sensations," in *Proceedings of the 10th International HAPTICS'02 Symposium*. IEEE, 2002, pp. 217–224.

[11] M. Salada, J.E.Colgate, P. Vishton, and E. Frankel, "Two experiments on the perception of slip at the fingertip," in *Proceedings of the 12th International HAPTICS'04 Symposium*. IEEE, March 2004.

[12] K. Kuchenbecker and W. Provancher, "Haptic display of contact location," in *Proceedings of the 12th International HAPTICS'04 Symposium*. IEEE, March 2004.

[13] M. Ernst and M. Banks, "Humans integrate visual and haptic information in a statistically optimal fashion," *Nature*, vol. 415, pp. 429–433, January 2002.

[14] A. Goodwin, *Neural Aspects of Tactile Sensation*. Elsevier Science, 1998, ch. Extracting the Shape of an Object from the Responses of Peripheral Nerve Fibers, pp. 55–87.

[15] F. Reynier and V. Hayward, "Summary of the kinesthetic and tactile function of the human upper extramities," McGill Research Centre for Intelligent Machines, Montreal, Tech. Rep., 1993.

[16] E. Goldstein, *Sensation and Perception*, 3rd ed. Brooks/Cole, 1989.

[17] K. Shimoga, "A survey of perceptual feedback issues in dexterous telemanipulation: Part II," in *Virtual Reality Annual International Symposium*, 1993, pp. 271–279.

[18] C. Youngblut, R. Johnston, S. Nash, R. Wienclaw, and C. Will, "Review of virtual environment interfaces technology," Institute for Defense Analyses (IDA), Tech. Rep., 1996.

[19] V. G. Macefield, *Neural Aspects of Tactile Sensation*. Elsevier Science, 1998, ch. The Signalling of Touch, Finger Movements and Manipulating Forces by Mechanoreceptors in Human Skin, pp. 89–130.

[20] R. Johansson and A. Vallbo, "Tactile sensory coding in the glabrous skin of the human hand," *Trends in NeuroSciences*, vol. 6, no. 1, pp. 27–32, Jan. 1983.

[21] R. Johansson and A. Vvallbo, "Tactile sensibility in the human hand: relative and absolute densities of four types of mechanoreceptive units in glabrous skin." *Journal of Physiology*, vol. 297, pp. 405–422, 1979.

[22] S. Biggs and M. Srinivasan, *Handbook of Virtual Environments*. Lawrence Earlbaum, Inc., 2002, ch. 5.

[23] ——, "Tangential versus normal displacements of skin: Relative effectiveness for producing tactile sensations," in *HAPTICS'02*. IEEE, 2002.

[24] R. Verrillo, "Effect of contactor area on the vibrotactile threshold," *The Journal of the Acoustical Society of America*, vol. 35, no. 12, pp. 1962–1966, 1963.

[25] G. Essick, "Factors affecting direction discrimination of moving tactile stimuli," *Neural Aspects of tactile sensation*, pp. 1–54, 1998.

[26] K. Johnson, T. Yoshioka, and F. Vega-Bermudez, "Tactile functions of mechanoreceptive afferents innervating the hand," *Journal of Clinical Neurophysiology*, vol. 17, no. 6, pp. 539–558, 2000.

[27] V. Hayward, "Tactile display device using distributed lateral skin stretch," in *Symposium on Haptic Interfaces for Virtual Environment and Teleoperator Systems*, Nov. 2000.

[28] P. Kammermeier and G. Schmidt, "Application-Specific Evaluation of Tactile Array Displays for the Human Fingertip," in *Proceedings of the 2002 IEEE/RSJ International Conference on Intelligent Robots and Systems IROS*, EPFL, Lausanne, Switzerland, 2002, pp. 2937–2942.

[29] G. Moy, "Human tactile spatial sensitivity for tactile feedback," in *Int. Conf. on Robotics & Automation*. IEEE, April 2000, pp. 776–782.

[30] M. Harders, A. Mazzone, G. Szekely, J. Citerin, M. Hafez, A. Kheddar, N. Sgambelluri, E. Scilingo, and A. Bicchi, "Deliverable 4.1: Preliminary report on physical principles," September 2003, `http://www.touch-hapsys.org`.

[31] P. Kammermeier, A. Kron, M. Buss, and G. Schmidt, "Towards Intuitive Multi-fingered Haptic Exploration and Manipulation," in *Proceedings of the 2001 Workshop on Advances in Multimodal Telepresence Systems*, Munich, Germany, 2001, pp. 57–70.

[32] C. Wagner, "A tactile display using RC servomotors," in *Symp. on Haptic Interfaces for Virtual Environment and Teleoperator Systems*, March 2002.

[33] C. Hasser and M. Daniels, "Tactile feedback with adaptive controller for a force-reflecting haptic display. part1: Design," in *Southern Biomedical Engineering Conference*. IEEE, Mar 1996, pp. 526–529.

[34] ——, "Tactile feedback with adaptive controller for a force-reflecting haptic display. part2: Improvements and evaluation," in *Southern Biomedical Engineering Conference*. IEEE, Mar 1996, pp. 530–533.

[35] P. Kammermeier, M. Buss, and G. Schmidt, "Dynamic Display of Distributed Tactile Shape Information by a Prototypical Actuator Array," in *Proceedings of the IEEE/RSJ International Conference on Intelligent Robots and Systems IROS*, Takamatsu, Japan, 2000.

[36] M. Lind, "Linear motion mineature actuators," in 2nd *Tampere International Conference on Machine Automation*, Sept. 1998.

[37] G. Moy, C. Wagner, and R. Fearing, "A compliant tactile display for teletaction," in *Int. Conf. on Robotics & Automation*. IEEE, April 2000, pp. 3409–3415.

[38] D. Caldwell, N. Tsagarakis, and C. Giesler, "An integrated tactile/shear feedback array for stimulation of finger mechanoreceptor," in *Conference on Robotics & Automation*. IEEE, May 1999, pp. 287–292.

[39] P. Taylor, A. Moser, and A. Creed, "The design and control of a tactile display based on shape memory alloys," in *Int. Conference on Robotics and Automation*. IEEE, April 1997.

[40] R. D. Howe, D. A. Kontarinis, and W. J. Peine, "Shape memory alloy actuator controller design for tactile displays," in *Conf. on Decision & Control*. IEEE, Dec. 1995, pp. 3540–3544.

[41] K. Ikuta, M. Tsukamoto, and S. Hirose, "Mathematical model and experimental verification of shape memory alloy for designing micro actuator," in *Proc. Micro Electro Mechanical Systems*. IEEE, Feb. 1991, pp. 103–108.

[42] D. Grant and V. Hayward, "Design of memory alloy actuator with high strain and variable structure control," in *IEEE int. Conference on Robotics and Automation*. IEEE, 1995, pp. 2305–2312.

[43] M. Siegel, "Tactile display development: The driving-force for tactile sensor development," in *Int. Workshop Haptic Virtual Environments and Their Applications*. IEEE, 2002, pp. 115–118.

[44] N. Asamura, N. Yokoyama, and H. Shinoda, "A method of selective stimulation to epidermal skin receptors for realistic touch feedback," in *Virtual Reality, 1999*. IEEE, March 1999, pp. 274–281.
[45] H. Ringhandt and C. Wirth, *Feinwerkelemente*. Carl Hansa Verlag, Muenchen, 1992.
[46] C. Kasuga, T. Nishimura, and F. Harashima, "Characteristics analysis method of multi-layer piezo-ceramic actuator simulation of equivalent circuit using the state space method," in *Proceedings of the 1992 International Conference on Power Electronics and Motion Control*, vol. 1, Nov. 1992, pp. 336–339.
[47] H. Czichos, Ed., *HÜTTE, Die Grundlagen der Ingenieurwissenschaften*, 31st ed. Springer, 2000.
[48] J. Lunze, *Regelungstechnik 2*, 2nd ed. Springer, 2002.
[49] G. Schmidt, "Regelung- und Steuerungstechnik 2," LSR Technische Universität München, Tech. Rep., 2000, lecture Notes.
[50] *Tutorial: Piezoelectrics in Positioning*, `http://www.physikinstrumente.de/`.
[51] M. Fritschi, "Deliverable 6.1: Design of a tactile shear force prototype display," March 2003, `http://www.touch-hapsys.org`.
[52] M. Fritschi, K. Drewing, R. Zopf, M. Ernst, and M. Buss, "Construction and first evaluation of a newly developed tactile shear force display," in *Proceedings of the EuroHaptics'2004 Conference*, Munich, Germany, 2004, pp. 508–511.
[53] D. Keyson and A. Houtsma, "Directional sensitivity to a tactile point stimulus moving across the fingerpad," *Perception & Psychophysics*, vol. 57, no. 5, pp. 738–744, 1995.
[54] F. Wichmann and N. Hill, "The psychometric function: I. filling, sampling and goodness-of-fit," *Perception and Psychophysics*, vol. 63, no. 8, pp. 1293–1313, 2001.